AIAA 2023-2024 Undergraduate Team Aircraft Design
Final Design Report

Team Kinglet - Gravibus

Matthew Brotnow, Lucas Smerica, Cynthia Sigamony, Eduardo Martinez, Jackson Long, Daniel Zapata, Yesung Jeon, & Vincent Ma

AE 443 - Aircraft Systems Design II
Department of Aerospace Engineering
University of Illinois, Urbana-Champaign
May 12, 2024

Matt Brotnow

Eduardo Martinez

Vincent Ma

Jackson Long

Lucas Smerica

Cynthia Sigamony

Yesung Jeon

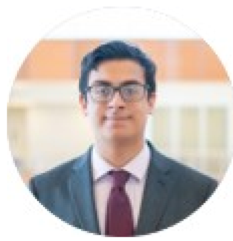

Daniel Zapata

Dr. Jason Merret

Team Kinglet Members

Team Member Contributions

Team Member	Primary Discipline(s)	Secondary Discipline(s)	AIAA Number	Signature
Matt Brotnow	Team Lead	Interior Design	1438174	[illegible]
Eduardo Martinez	Aerodynamics	Certification	1180797	[illegible]
Vincent Ma	Structures	Acoustics & Emissions	1602084	Vincent Ma
Jackson Long	Systems & Mass Props	Repair & Maintenance	1602082	[illegible]
Lucas Smerica	Propulsion	Landing Gear	1536795	[illegible]
Cynthia Sigamony	Performance	Configuration	1400177	[illegible]
Yesung Jeon	Loads & Dynamics	Cost	1404858	[illegible]
Daniel Zapata	Stability and Control	Avionics	1595303	[illegible]
Dr. Jason Merret	Faculty Advisor	-	155270	

Contents

List of Figures

List of Tables

Nomenclature

AR	=	Aspect Ratio
C	=	Chord
C_D	=	Drag Coefficient
C_{HT}, C_{VT}	=	Tail Coefficients
C_L	=	Lift Coefficient
C_m	=	Moment Coefficient
e_o	=	Oswalds Efficiency
g	=	Acceleration due to gravity
K	=	Constant
L/D	=	Lift-to-drag Ratio
M	=	Mach Number
q	=	Dynamic Pressure
Re	=	Reynolds Number
S	=	Area, Distance
T	=	Thrust
V	=	Velocity
W	=	Weight
α	=	Angle of Attack
δ	=	Deflection Angle
λ	=	Taper Ratio
μ	=	Friction Coefficient
σ	=	Stress, Density Ratio

Acronyms

AIAA	=	American Institute of Aeronautics and Astronautics
AVL	=	Athena Vortex Lattice
BFL	=	Balanced Field Length
BWB	=	Blended Wing Body
CFD	=	Computational Fluid Dynamics
CFR	=	Code of Federal Regulations
CG	=	Center of Gravity
CPI	=	Consumer Price Index
DC	=	Direct Current
ISA	=	International Standard Atmosphere
EASA	=	European Union Aviation Safety Agency
ECS	=	Environmental Control System
EIS	=	Entry Into Service
FAA	=	Federal Aviation Administration
FAR	=	Federal Aviation Regulations
FEA	=	Finite Element Analysis
GPS	=	Global Positioning Satellite
HLA	=	Heavy Lift Aircraft
HPC	=	High Pressure Compressor
HPT	=	High Pressure Turbine
HSC	=	Home Station Check
ICAO	=	International Civil Aviation Organization
IDG	=	Integrated Drive Generator
IFF	=	Identification Friend or Foe
INS	=	Inertial Navigation System
LEDAC	=	Low Emission Dual Annular Combustor
LFL	=	Landing Field Length
LPC	=	Low Pressure Compressor
LPT	=	Low Pressure Turbine
LRU	=	Line Removable Unit
MAC	=	Mean Aerodynamic Chord
MMH/FH	=	Maintenance Man Hours per Flight Hour
MTOW	=	Maximum Takeoff Weight
PMG	=	Permanent Magnet Generator
RDTE	=	Research Development Test and Evaluation
RFP	=	Request for Proposal
ROC	=	Rate of Climb
SATCOM	=	Satellite Communications
SDAC	=	Standard Dual Annular Combustor
SFC	=	Specific Fuel Consumption
TACAN	=	Tactical Air Navigation System
TFR	=	Terrain-Following Radar
TO	=	Takeoff
TOC	=	Top of Climb
TOFL	=	Takeoff Field Length
TW	=	Tube Wing
USAF	=	United States Air Force
USD	=	United States Dollar
VHF	=	Very High Frequency
VSCF	=	Variable Speed Constant Frequency
VTAS	=	Velocity True Airspeed
WUTTO	=	Warm Up, Taxi, and Takeoff

Compliance Checklist

The AIAA request for proposal outlines many mandatory and tradable requirements [1]. The compliance checklist in the table below outlines the major requirements, Gravibus' corresponding characteristic(s), and points to where in the report that requirement is discussed.

Gravibus Compliance Checklist

Description	Requirement	Gravibus	Section
Entry Into Service	2033	2033	II.A
Powerplant Entry Into Service	2029	1995	V.A.3
Maximum Payload	430,000 lbs	430,000 lbs	VI.B
M1A2 Main Battle Tank Capacity	3	3	IV.A
463L Pallet Capacity	48	50 (by volume)	IV.A
Fully Equipped Troop Capacity	330	330	IV.A
Separate Troop Compartment Capacity	100	100	IV.A
Cruise Mach Speed Range	0.80 - 0.82	0.80 - 0.82	VI.B
Range at 430,000 lb Payload	2,500 nmi	2,500 nmi	VI.B
Range at 295,000 lb Payload	5,000 nmi	5,000 nmi	VI.B
Range at 0 lb Payload	8,000 nmi	8,000 nmi	VI.B
Initial Cruise Altitude	≥ 31,000 feet	31,000 feet	VI.B
Service Ceiling	≥ 43,000 feet	45,440 feet	VI.E
Field Length on +15 DISA Day	≤ 9,000 feet	8,790 feet	VI.A
Wingspan	ICAO Code F (≤ 80 m)	262 feet (80 m)	IV

Executive Summary

Heavy-lift aircraft represent a key strategic piece in the ability of the United States Air Force to effectively deploy and sustain forces anywhere in the world. The current HLAs, the C-5M and the C-17, are maturing and will be replaced within the coming decades [1].The request for proposal requires an HLA that, at a minimum, can transport 100 fully equipped troops in a separate bay and 3 M1A2 Abrams Main Battle Tanks, 48 463L pallets, or 330 additional troops [1]. The aircraft must also operate from a 9,000-foot runway and travel 5,000 nautical miles with a payload of 295,000 pounds. The table below outlines some key parameters of the team's proposed aircraft, Gravibus.

Design Summary

Metric	Value	Metric	Value
Maximum Takeoff Weight	1,160,000 lbs	Maximum Fuel Weight	389,000 lbs
Wing Area	6,000 sq. ft	Aspect Ratio	11.5
Wing Configuration	High wing	Tail Configuration	Twin Tail
Wing Span	262 ft	Length	279 ft
Engines	GE90-85B	Number of Engines	4
Cruise Speed	270 kts	Cruise Altitude	31,000 ft

The design of Gravibus began with understanding all the operational requirements of the aircraft, including the three nominal missions and the cargo handling capabilities. Next, initial sizing took place to generate high-level requirements for weights and key performance metrics. The internal configuration was then developed to satisfy the cargo requirements, and then the outer mold line was fitted around the cargo bay. Detailed design and analysis then began in parallel for propulsion, performance, aerodynamics, mass properties, and all other disciplines with the use of computational and empirical tools. Trades, design loops, and iterative design took place with heavy collaboration between disciplines. The final result of this design process is Gravibus.

Gravibus is a high-wing, twin tail blended wing body aircraft powered by four GE90-85B engines. The outer mold line was driven by volumetric constraints from the cargo capacity, and wing and engine sizes were driven through the 9,000-foot field length requirement while minimizing the fuel needed for the three missions. The adoption of the blended wing body design allows for lowering operating costs, namely $ 247,218,150,000 per year, which helps differentiate it from other proposed aircraft and from the C-5.

I. Introduction

The United States Air Force (USAF) must maintain the ability to deploy and sustain forces effectively and rapidly around the world. Heavy-lift aircraft (HLA) are a key component of this ability, and the current HLAs, the C-17 and C-5M, are maturing and will require replacement within the coming decades [1]. Thus, the AIAA request for proposal (RFP) calls for an aircraft that can effectively replace these aircraft with greater cargo capacity and range capabilities. This report contains the design and analysis of a novel blended wing body (BWB) aircraft, Gravibus, that satisfies all requirements set forth by the RFP. Some key requirements include operating from a 9,000-foot runway and the three payload-range requirements: 2,500 nmi at the maximum payload of 430,000 lbs, 5,000 nmi at 295,000 lb payload, and an 8,000 nmi ferry range. On top of the base requirements, one key advantage of adopting a blended wing body design is a direct reduction in operating costs in the form of reduced fuel consumption. Gravibus will cost $ 76,500 per flight hour to operate, which is significantly less than its predecessor the C-5M. Table 1 details key characteristics of Gravibus and Fig. 1 shows a rendering of Gravibus.

Table 1 Key Characteristics

Metric	Value	Metric	Value
MTOW	1,160,000 lbs	Empty Weight	475,000 lbs
Wing Area	6,000 sq. ft	Aspect Ratio	11.5
Wing Span	262 ft	Overall Length	279 ft
Engines	4 GE90-85B	Max Takeoff Thrust	326,000 lbs
Range at Max Payload	2,500 nmi	Service Ceiling	45,440 ft
Takeoff Field Length	8,550 ft	Landing Field Length	8,790 ft

Fig. 1 Gravibus Render

II. Concept of Operations

A. Requirements

The main operations of the HLA are clearly laid out by the RFP: the aircraft must have an unrefueled range of no less than 2,500 nmi at maximum payload, it must be able to achieve 5,000 nmi at a payload of 295,000 lbs, and a ferry range of at least 8,000 nmi [1]. Other key requirements from the RFP include takeoff, cargo capacity, and entry into service (EIS) dates. For EIS, there are no technologies limiting the manufacture of Gravibus, so 2033 should be accomplished. Table 2 details some of these key RFP requirements and derived and allocated requirements that are taken from the RFP requirements. The cargo dimensions were determined by the largest of the three cargo requirements, which was the forty-eight 463L pallets. The thrust and C_L requirements were taken from the sizing analysis and will be expanded on in Section III.E.

Table 2 Design Requirements

RFP Requirement	Derived Requirements	Allocated Requirements
9,000 ft Field Length	326,600 lbs TO Thrust 2.0 $C_{L,max}$ at TO	Four Engines with 82,000 lbs thrust
Compatible with ICAO F Airport	80 m (262 ft) span limitation	Maximum AR per S_{ref}
48 463L Pallets	Minimum cargo bay of 3,168 sq. ft	118 by 45 ft main cargo bay
Separate bay for 100 troops	Minimum 322 sq. ft additional space	16 by 45 ft additional bay
EIS by 2033	-	Use current avionics/systems
Powerplant EIS by 2029	-	Use current powerplant

B. Design Missions & Operation

The operations of a heavy-lift cargo aircraft are consistent: load outsized or heavy cargo, fly to a base or forward operating point, and unload efficiently. Another key operations consideration is the repair and maintenance of the aircraft. Every aircraft produced will be operated out of its own "home base" in which repair and maintenance would be centralized. This would allow for replacement parts to be stored efficiently, and it would make maintenance schedules easier to coordinate. Larger overhauls, including Line C and D repairs, would take place at the home base specifically, to again make part storage and scheduling easier. Further repair and maintenance considerations are discussed in Section XIV. The HLA also has the capability of refueling mid-air, meaning it can fly anywhere in the world with support, and the aircraft will constantly be interacting and communicating with satellites and control centers. Figure 2 depicts all of the key interactions between Gravibus and the systems surrounding it.

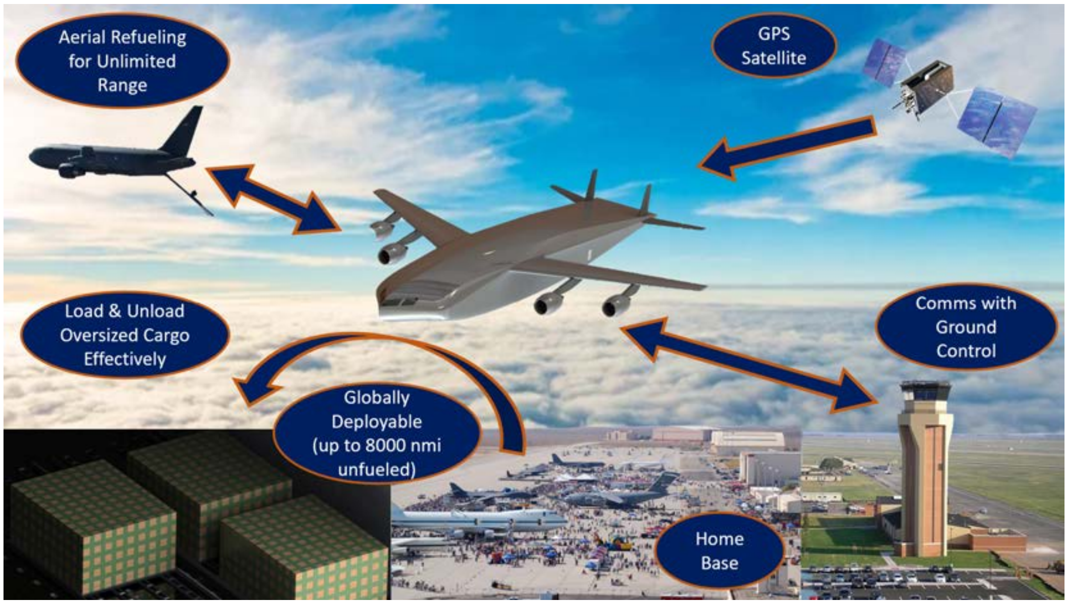

Fig. 2 OV-1 Diagram

Further, the three main missions set forth by the RFP are the three "Supply-Range" missions, as defined by MIL-STD-3013 [2]. These three missions are separated by their range per payload: 2,500 nmi at 430,000 lb payload, 5,000 nmi at 295,000 lbs, and 8,000 nmi ferry range [1]. MIL-STD-3013 also defines the reserves segment as 5% of initial fuel plus a 30-minute loiter [2]. Figure 3 and Table 3 visually depict the Supply-Range mission as well as details for each segment.

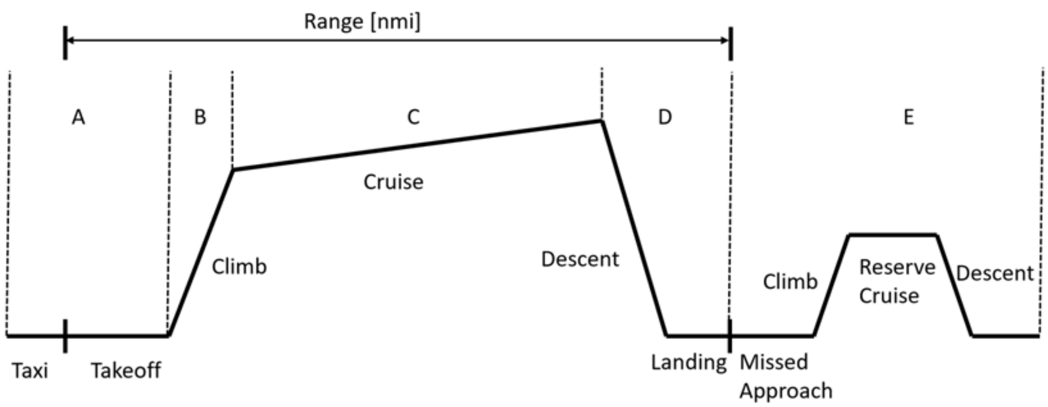

Fig. 3 Mission Profile

Table 3 Mission Segments

Segment	Description	Notes
A	Warm-Up, Takeoff, Accelerate to Climb Speed	20 minutes at idle, 30 second TO
B	Climb	Takeoff to Optimum Cruise
C	Cruise	2,500 nmi; 5,000 nmi; or 8,000 nmi
D	Descent	End of Cruise to Landing
E	Reserves	30 minutes and 5% of initial fuel

C. Conversion to Commercial Aviation

One final operational consideration is the conversion of Gravibus from a military cargo transport to a commercial aviation plane. The RFP states that while the primary market will be the US military and allies, a small number of aircraft should be marketed to non-USAF customers for a stronger economic argument [1]. The easiest conversion to a commercial aircraft would be to commercial transport carriers as this would not carry as many additional FAA requirements as compared to a commercial variation. The cargo bay may have to be slightly modified to align with the current commercial systems. Additional requirements that may have to be satisfied if the aircraft was converted to a passenger variation would be egress regulations such as CFR § 25.810. Yet, the conversion to a commercial cargo aircraft would not be as difficult, meaning that Gravibus is well-suited to be marketed and sold effectively.

III. Sizing Analysis

A. Constraint Analysis

After understanding the operations of the aircraft per the RFP requirements, the next step in the design process was understanding what values of thrust-to-weight and wing loading were possible for the team's design. Thrust-to-weight and wing loading are key parameters that give an idea of the relative size requirements of the aircraft. These parameters were analyzed for takeoff, landing, cruise, service ceiling, and loiter.

For takeoff, Raymer Eqn. (5.8) allows one to calculate the minimum wing loading needed to takeoff from a required field length for a given thrust-to-weight [3]. Any values of wing loading greater than those calculated would provide enough lift to takeoff in less than the required distance. For landing, maximum wing loading is calculated as wing loading effects approach speed and thus the kinetic energy associated with landing. Using Raymer Eq. (5.11), one can find the maximum wing loading, which is then scaled to maximum takeoff conditions [3]. Thus, any wing loading greater than the calculated value is a valid design that will be able to meet the landing distance requirement.

The cruise thrust-to-weight required is calculated using Raymer Eq. (5.3) and (5.4), which represent the minimum thrust-to-weight to provide a required climb gradient at cruise altitude [3]. Any thrust-to-weight greater than that calculated will satisfy this climb requirement. The wing loading required to fly at the service ceiling is calculated using Raymer Eq (5.33), and any wing loading greater than this will provide enough lift at the ceiling [3]. Finally, the wing loading for optimal loiter is calculated using Raymer Eq. (5.15) [3]. This value represents a design point optimized for loiter, not a requirement, but it is still useful to understand the general performance of the aircraft. Inputs for all equations were taken from similarity, were assumed, or were taken from Raymer Chapter 5 [3]. Table 4 summarizes the values with associated justification.

Table 4 Constraint Analysis Parameters

Parameter	Value	Justification
Takeoff Parameter	300 lb/sq.ft	Assumed for 4 engine from Raymer Fig. 5.4 [3]
σ	0.9505	Calculated for standard atmosphere at RFP takeoff condition
$C_{L,max}$ Takeoff	2.25	Assumed from similarity analysis
$(L/D)_{cruise}$	21	Calculated from Raymer Eq. (3.12) [3]
ROC	300 fpm	Cruise ROC requirement from MIL-STD-3013 [2]
Cruise VTAS	775 fps	Calculated from RFP requirements
W_{cruise}/W_{TO}	0.97	Assumed from Raymer Table 3.2 [3]
T_{TO}/T_{cruise}	4.55	Raymer Fig. 5.1 using RFP required altitude [3]
$q_{ceiling}$	152 psf	Calculated from RFP requirement
$C_{L,\ cruise}$	0.6	Calculated during initial sizing
q_{loiter}	51 psf	Recommendation from Raymer chapter five [3]
AR	11.5	Design Decision
e_o	0.85	Typical value taken from Raymer [3]
C_{D_0}	0.025	Assumed from similarity analysis
W_{loiter}/W_{TO}	0.85	Typical Value from Raymer chapter five [3]
$K_{landing}$	80	Raymer Eq. (5.11) [3]
$S_{landing}$	9,000 ft	RFP requirement
$C_{L,max}$ Landing	2.5	Assumed from similarity analysis
S_{air}	1000 ft	Typical Value from Raymer [3]

Using the equations described above, one can then construct a constraint diagram which depicts all combinations of wing loading and thrust-to-weight that would produce a valid design. Figure 4 depicts the constraint diagram with the valid design region shaded in green and where Gravibus falls is marked with a star. Notice that the design point falls on the takeoff line which reinforces the idea that takeoff is the mission segment that constrains the aircraft the most. Ideally, the design point would fall further towards the bottom left corner of the valid design region, which would require a larger wing and smaller engines. Typically the increased initial cost associated with a larger wing would be offset by the continual cost savings from using a smaller engines. However, the constraint diagram only uses relative wing size and thrust values which are scaled with weight. Once actual weight values were used, the ICAO Code F span limitations limited the practical limits of the wing area, which moved the design point to where it is marked.

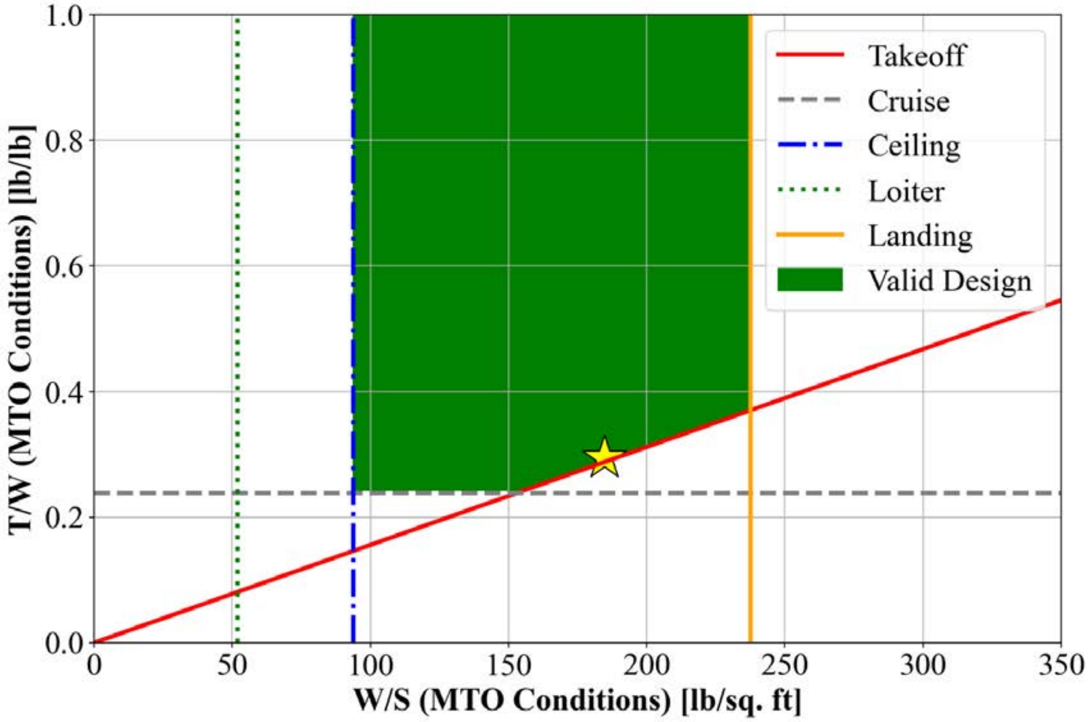

Fig. 4 Constraint Diagram

B. Similarity Analysis

Another important step in the design process is to evaluate and analyze aircraft within the same class, which is heavy-lift aircraft for the purposes of this report. Two aircraft which have a large amount of data that is publicly available in the HLA class are the Lockheed C-5 and the Boeing 747. The data collected are used to calibrate portions of the initial sizing process and to serve as a general benchmark against Gravibus. Data for the C-5 was from Lockheed Martin and the USAF [4, 5]. The 747 data was from a Boeing publication [6]. All the collected parameters are summarized in Table 5.

Table 5 Similarity Data

Parameter	C-5M	747-400	Parameter	C-5M	747-400
MTOW [lbs]	840,000	875,000	Empty Weight [lbs]	380,000	360,900
Fuel Weight [lbs]	332,500	265,000	Max Landing Weight [lbs]	635,850	652,000
Wing Area [sq. ft]	6,200	5,825	Span [ft]	223	211
C/4 Sweep [°]	25	39	Taper	0.387	0.212
Fuselage Length [in]	2,974	2,782	Cruise Altitude [ft]	33,000	34,600
Mach at Cruise	0.77	0.845	Takeoff Field Length [ft]	8,300	10,200
Horizontal Tail Area [sq. ft]	985	1,248	Vertical Tail Area [sq. ft]	952	845
Number of Engines	4	4	Takeoff Thrust Per Engine [lb]	51,250	62,100

C. Blended Wing Body or Tube Wing

After collecting data from similar class aircraft, the team then began the design process. The first major decision was whether to pursue a blended wing body (BWB) or tube wing (TW) design. To evaluate this decision, independent sizing loops were conducted for both the BWB and TW configurations due to the fact that the weight equations used were very different. Both sizing loops were iterated until they were able to meet the range requirement of the 295,000 lb - 5,000 nmi mission and the 9,000 foot runway requirement. The sizing loops were then swept across aspect ratios from 6 to 15 and wing areas from 5,000 to 10,000 sq. ft. Figure 5 depicts the fuel weight plots for both the BWB and TW designs.

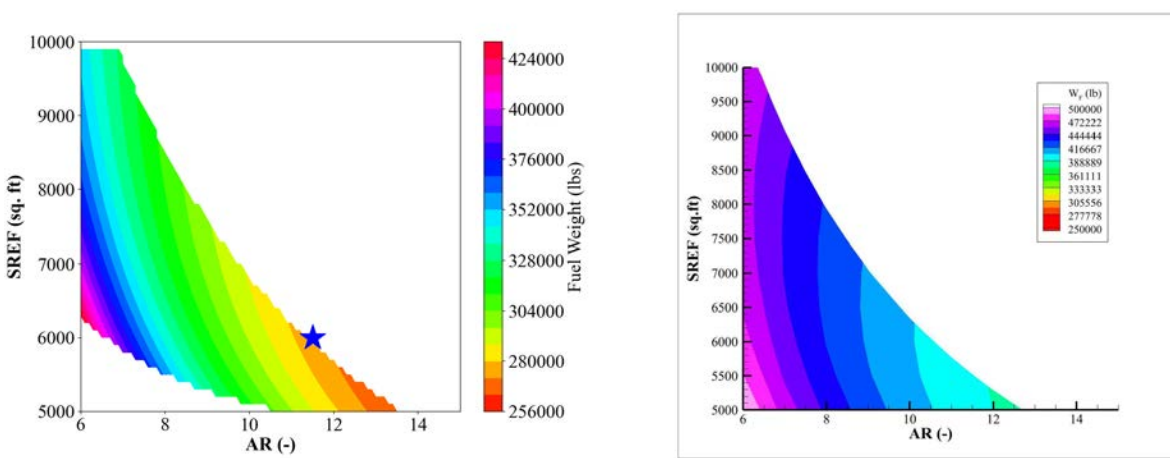

Fig. 5 Fuel Weight Comparison of BWB (left) and TW (right) Configurations

Examining these plots closer, one can see that overall the BWB design shows significant fuel savings. In particular, if the AR of 11.5 and wing area of 6,000 sq. ft are taken from both plots, the reduction in fuel is 24.43 %. Similar trends can be seen in many other parameters, such as takeoff thrust required, which showed a 25.21 % reduction by adopting a BWB design. From these plots, as well as a general comparison between a BWB and TW design, the BWB configuration would result in lower costs. A reduction in fuel consumed directly results in lower operating costs, and a reduction in takeoff thrust can increase the engine lifespan and reduce maintenance costs, both of which lower the life cycle costs of the aircraft. Another key benefit of the BWB design is a reduction in wing weight. The 'fuselage' section of the BWB produces significant amounts of lift, reducing the percent of the lift that needs to be produced by the outer wing. Thus, since the wing does not need to produce as much lift, the structure to counteract the lift distribution can be reduced significantly. Reducing the weight of the structures reduces manufacturing costs as well as all of the additional benefits of reduced empty weight. For these reasons and others, the team thus chose to pursue a BWB design for Gravibus.

D. Number of Engines Trade

Another important trade conducted before the final initial sizing loop was conducted was on the number of engines. The majority of HLA utilize a four engine configuration with some going to a six engine configuration. Thus, for this trade, sizing loops with both four and six engines were considered. Again, they were converged to meet the 295,000 lb - 5,000 nmi mission and the 9,000 foot runway requirement, and they were again swept over aspect ratios between 6 and 15 and wing areas between 5,000 and 10,000 sq. ft. Figure 6 depicts the fuel weight plots for both the four and six engine sizing loops.

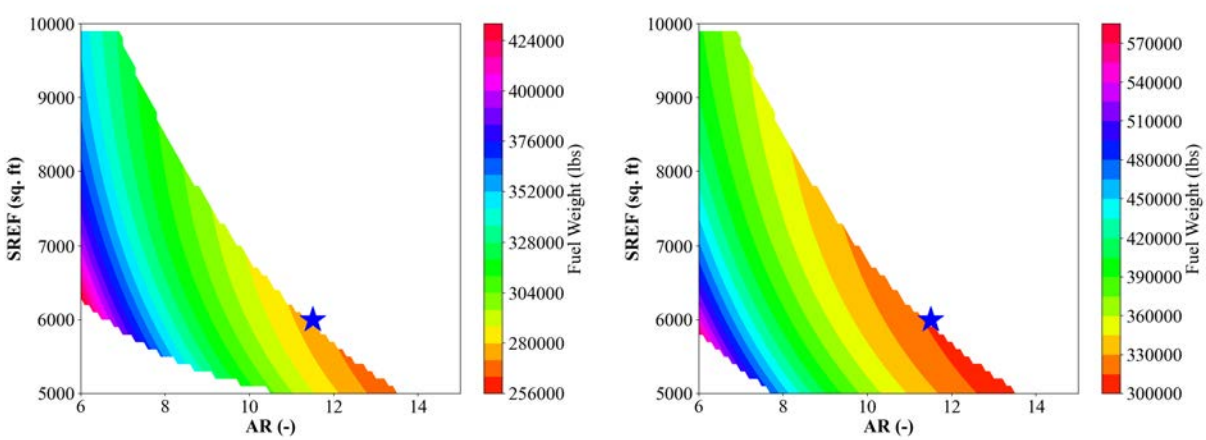

Fig. 6 Fuel Weight Comparison of Four Engine (left) and Six Engine (right) Configurations

From Fig. 6, one can see that the fuel weights are larger for the six engine configuration, implying that any benefits seen from takeoff performance are lost during cruise or from the added weight associated with additional engines. If the design point of an AR of 11.5 and wing area of 6,000 sq. ft is again examined, the fuel weight increases 5.52 % and the empty weight increases 6.61 % going from a four to a six engine configuration. Additional engines would likely incur increased maintenance costs and other costs. Thus, Gravibus will feature a four engine configuration.

E. Aircraft Initial Sizing

After conducting these two trade studies, the initial sizing of Gravibus could then be completed. The sizing loop was based on a part-by-part weight build up for a BWB aircraft courtesy of D. Howe of Cranfield University [7]. The weights are split into an outer and inner wing with additional penalties for the inner wing for items such as the cargo bay floor. The weight build up was paired with a drag build up based on Raymer Chapter 12 [3]. The sizing loop required some key constants, such as the number of engines, the cargo bay dimensions, specific fuel consumption, and $C_{L,\,max}$ at takeoff, to be input, as well as first guesses for the thrust required from each engine and fuel weight. Then, the loop calculated the range equation and takeoff equation from Raymer Chapter 5 [3], adjusted the thrust and fuel weight, and recalculated the equations until the values converged. Then, the loop swept over aspect ratios from 6 to 10 and wing areas from 5,000 to 10,000 sq.ft. To ensure all three missions were met, the 295,000 lb mission and 430,000 lb mission were calculated independently and used to find the greatest maximum empty and takeoff weight. Then, these values were used to determine fuel weight for all three missions and to verify that all performance requirements were met. Figure 7 visually depicts this process, and Fig. 8 depicts the fuel weight plots for the 295,000 lb and 430,000 lb missions. The chosen design point is marked with a blue star and areas of the plot where the ICAO span limitation were not satisfied are blanked.

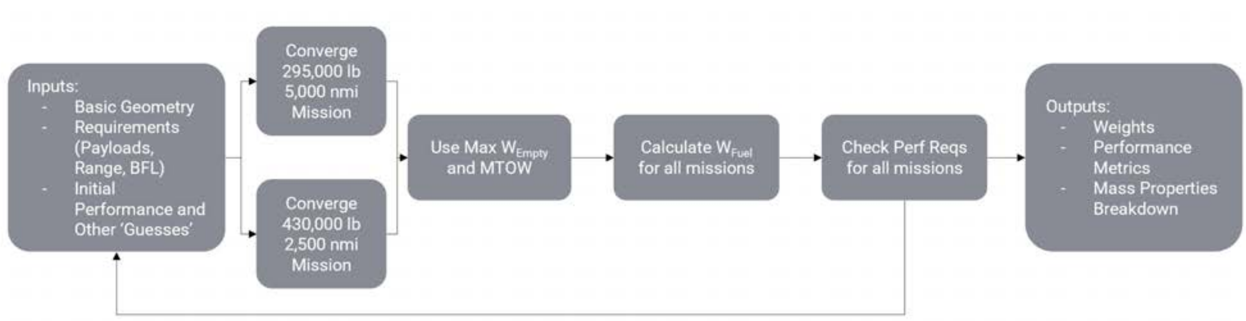

Fig. 7 Sizing Loop Process

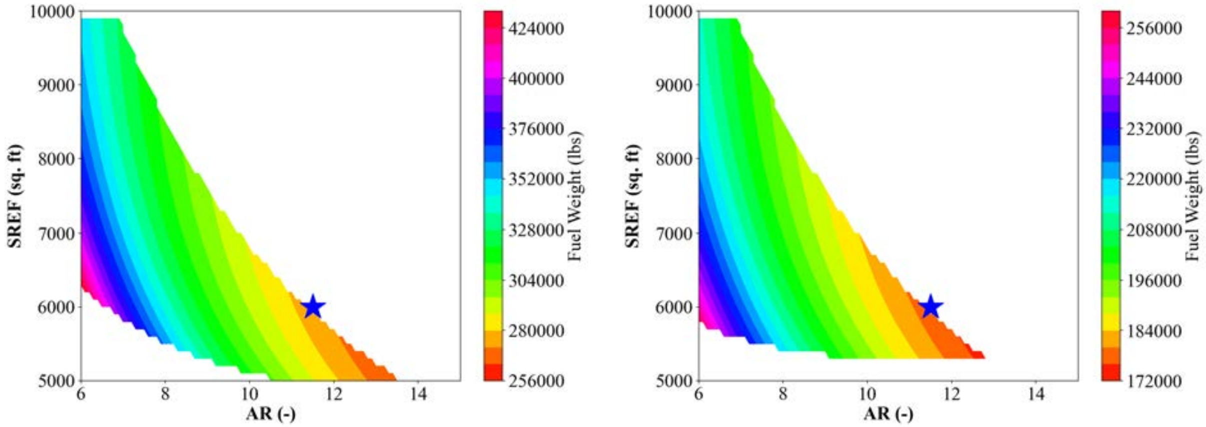

Fig. 8 Fuel Weight Plots for 295K (left) and 430K (right) Missions

When selecting a design point, minimizing fuel weight was the primary objective, as a reduction in fuel directly results in lower operating costs. However, there must be a minimum amount of wing volume for fuel storage and systems integration, which led to the chosen design point of a wing area of 6,000 sq. ft and an aspect ratio of 11.5. Throughout the sizing process, requirements can be derived and allocated to guide the next steps of the design process. Some of these key requirements are summarized in Table 6.

Table 6 Sizing Derived Requirements

Parameter	Value	Justification	Requirement Type
Maximum Span	262 ft	ICAO Code F Airport	Allocated
Minimum W/S TO	94 psf	Constraint Diagram	Derived
$C_{L,max}$ Takeoff	2.0	Similarity analysis	Derived
Takeoff Thrust (per engine)	81,653 lbs	Output from Sizing	Derived

IV. Configuration

A. Internal Configuration Design

As the cargo bay requirements drive the overall size and outer mold line of the aircraft, the interiors were designed first. The three nominal cargo requirements from the RFP are 3 M1A2 Abrams Main Battle Tanks, 48 463L pallets, and 330 fully equipped troops in addition to a separate bay for 100 troops [1]. The cargo floor area was driven by the largest of the three required cargo capacities; the 48 pallets were the largest and sized the floor at 118 ft by 45 ft. The pallets are configured in a 5 x 10 layout, meaning two additional pallets can be carried if the total weight stays below 430,000 lbs. The 330 passengers will be seated in six columns of fifty-five, and the three Abrams are configured in a triangular fashion. The one hundred additional troops will sit forward of the main cargo bay, split into two floors with five rows of ten each. In accordance with the RFP, Gravibus must also be capable of carrying any cargo similar to the C-5. By volume, Gravibus can carry: 4 CH-47 Chinooks, 4 AH-64 Apaches, 35 Humvees, or 8 M198 Howitzers. Figure 9 depicts the three main cargo configurations with dimensions.

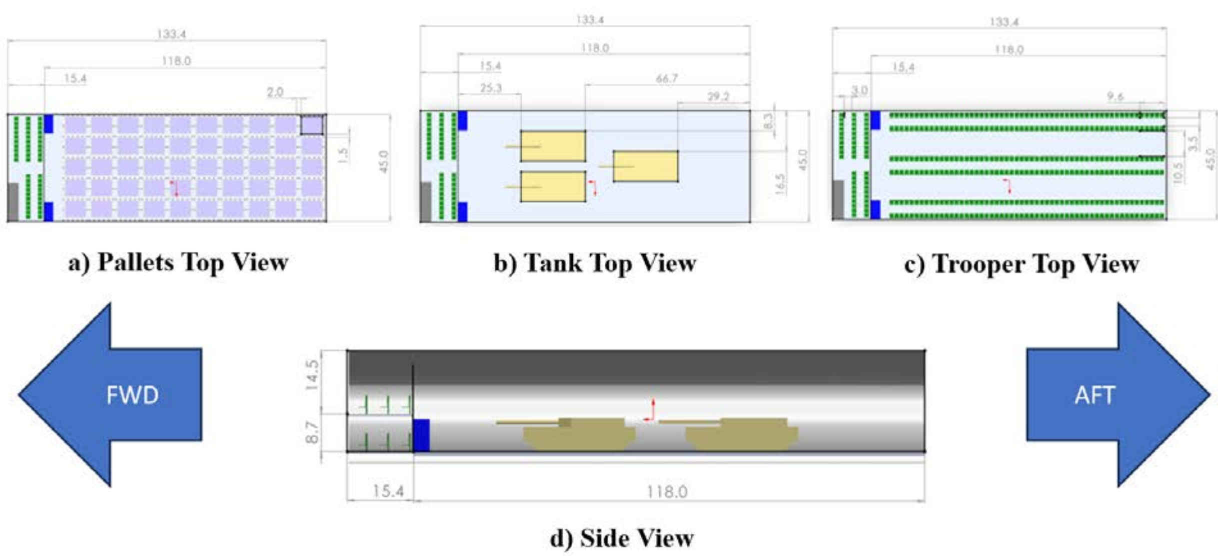

Fig. 9 Interior Configurations (dimensions in feet)

Additional internal configuration items include the cargo ramp, crew rest quarters, the flight deck, and miscellaneous items such as staircases and bathrooms. The cargo ramp spans the entire width of the cargo bay allowing for the minimum one point of outsized cargo loading access, and the length of 51 feet allows the 12 °ramp angle requirement to met be exactly [1]. The flight deck will be discussed further in Section XIII.A. The crew rest area and flight deck are directly forward of the second floor of the passenger bay, separated by doors that are able to be locked. The crew rest areas provide sufficient room for the four relief crew members and complies with FAA AC-117-1 [8]. The flight deck, crew rest area, and second floor of the passenger area are all accessible via a central staircase designed in accordance with the FAA Human Factors Design Standard Chapter 10 [9]. Figure 10 depicts the entire layout of the interior including the flight deck and crew rest area.

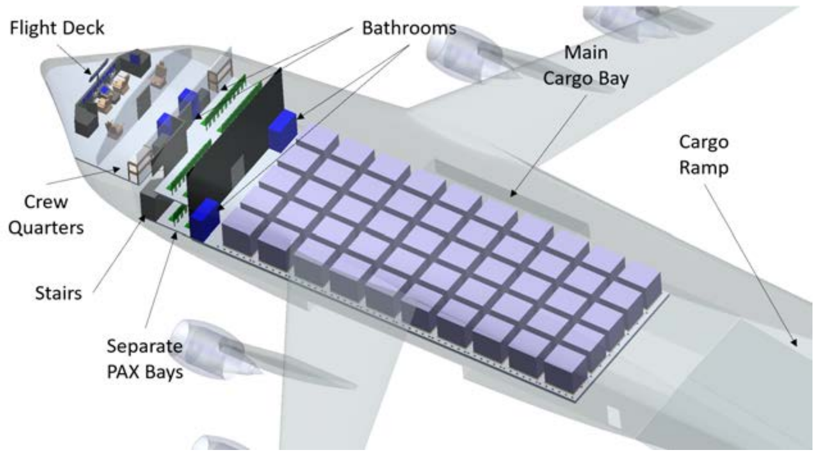

Fig. 10 Interior Layout

Further, the operations surrounding the cargo loading, unloading, and restraint are critical. As such, systems similar to the C-5 and C-17 were implemented for pallets and tie downs to ensure an easy transition from these aircraft to Gravibus and allow the aircraft to be loaded and unloaded rapidly. In particular, the rail and roller system are designed to the Army Materiel Command specifications [10], and the tie down and restraints are designed in accordance with MIL-STD-209 and AD-768 389 [11, 12]. These systems are depicted below in Fig. 11.

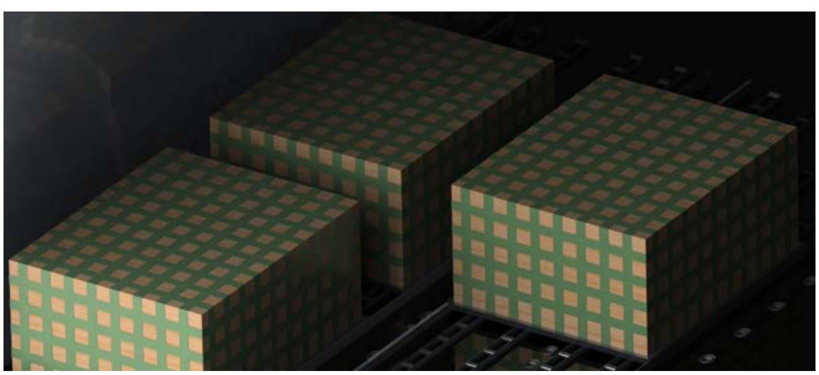

Fig. 11 Rail, Roller, and Restraint Systems

B. External Configuration Alternatives

When considering external configuration alternatives the team initially investigated a traditional tube-wing body. However, after in depth trade studies, the team decided to pursue a BWB configuration. Initial BWB configurations included different engine mounts, shown in Fig. 12. Further advantages and disadvantages between these alternatives will be discussed in Section V.C.1.

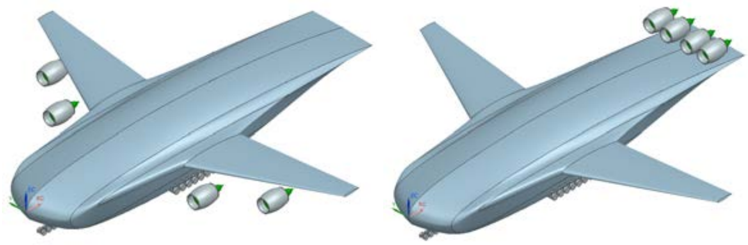

Fig. 12 Engine Configuration Alternatives

Further external configurations were considered, and can be seen in Fig. 13. A high wing configuration was chosen for its ability to generate more lift. When running these models in computational fluid dynamics software, CD_i and CD_o values were determined to be much lower for the nose configuration on the right, than the one on the left of Fig. 13. In addition, the rear tail tips were removed for the final design, as they produced extra drag. Once the nose, wing and engines were placed, the horizontal and vertical stabilizers were sized. A twin tail design was chosen over a single tail design as it was more structurally sound.

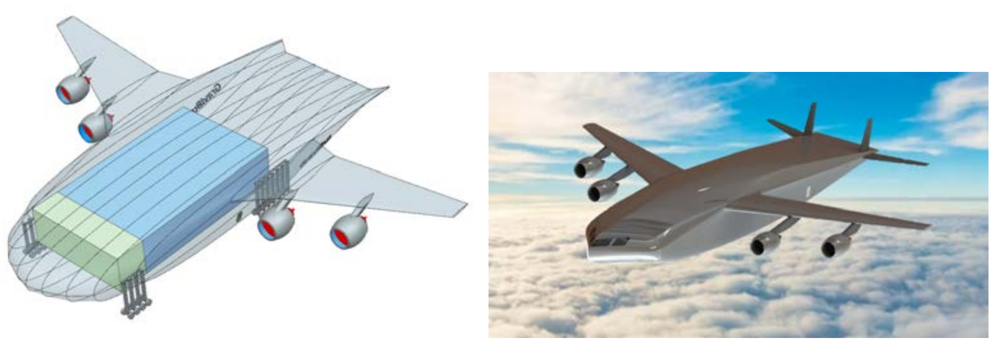

Fig. 13 Initial external configuration and chosen external configuration

C. Selected Aircraft Configuration

A tool was created to aid in the placement of airfoils for the main body of the Gravibus. A center chord airfoil was placed at the center of the cargo bay and moulded around it. To complete the main body, a 'baychord' airfoil was chosen to be placed at a few inches just beyond the maximum width of the cargo bay to allow room for the pressure vessel. Values for wing dimensions were set by initial sizing. Next, airfoils for the wing root and tip were placed at locations on the main body determined by the required area from initial sizing, and to minimize CG variance with different loading conditions. The wing geometry was varied with a small transition space to blend the main body and wings together for desired aerodynamic characteristics, as well as for aesthetic purposes. These variations were then iterated alongside sizing and aerodynamics until the whole body geometry matched calculated values. Two paratrooper doors were placed on either side of the aircraft, behind the wings. This allows plenty of room for paratroopers to jump safely out of the aircraft during flight. Table 7 shows significant dimensions of the team's selected configuration. A dimensioned three view drawing of the Gravibus can be seen on the following page, in figure 14.

Table 7 Selected Aircraft Dimensions

Parameter	Value	Units
Outer Wing Area	5,314	ft^2
Reference Area	6,000	ft^2
Total Span	262	ft
Outer Wing AR	8.1	-
Outer Sweep	25	degrees
Wing taper ratio	0.3	-
Center Chord	270	ft
Distance from Center Chord to Baychord	22.5	ft
Root Chord	39.5	ft
Tip Chord	13.3	ft
Length of main body	279	ft
Height of main body	35	ft

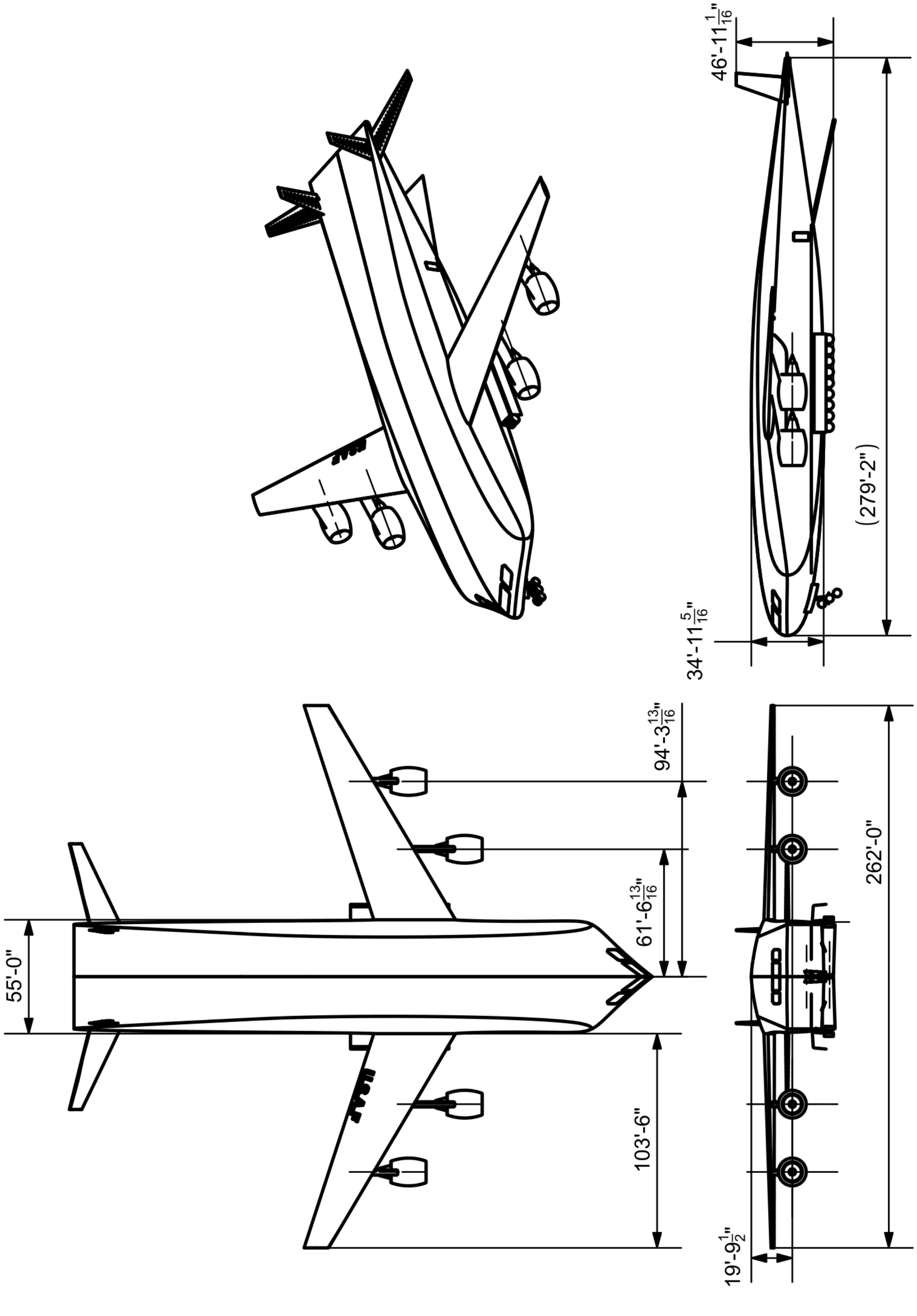

Fig. 14 Three-view of the Gravibus with dimensions and an isometric view

V. Propulsion

A. Engine Selection

1. Engine System

The RFP specifies that the HLA be powered by air breathing powerplants and that the HLA must cruise between 31,000ft and 43,000ft in altitude at speeds between Mach 0.80 to 0.82 [1]. Given these requirements, it was determined that a high-bypass turbofan jet engine would be used to propel Gravibus. This decision is supported by Fig. 15 found in Chapter 3 of El-Sayed [13], which shows that at cruise Mach numbers of 0.80 to 0.820 (approximately 600 to 630 miles per hour) the high-bypass turbofan engine is the most efficient propulsive system.

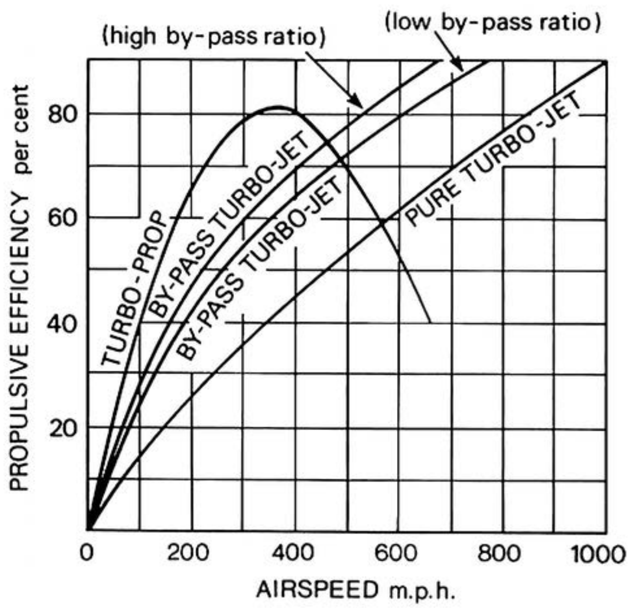

Fig. 15 Propulsive System Efficiencies

A turbofan works by compressing incoming air through its fan, low-pressure compressor, and high-pressure compressor. Then, the compressed air is mixed with fuel and ignited. Lastly, the hot, high-pressure gas drives the high-pressure and low-pressure turbines as it escapes at high velocity through the nozzle. Figure 16 illustrates the system of a turbofan engine, as adapted from [14]. The ratio of mass flows between the air going through the fan and the air going into the engine core is called the bypass ratio. High bypass engines are able to produce sizable amounts of thrust at subsonic speeds while featuring better fuel efficiencies.

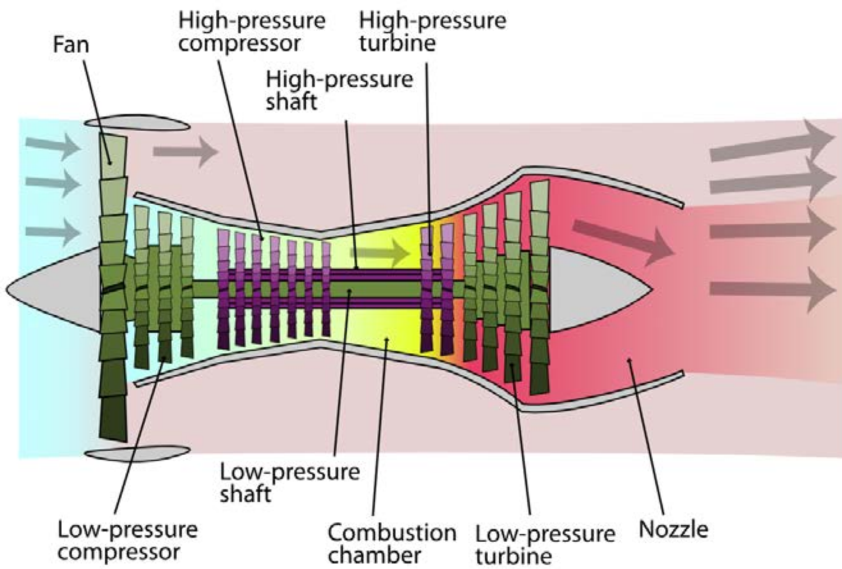

Fig. 16 Turbofan System

2. Propulsive Requirements

Certain engine performance requirements were given during the initial sizing. Assuming a 4-engine configuration, the thrust required at various conditions is given in Table 8. The RFP requirement that the powerplant be "currently in service or anticipated to enter service within the next 5 years" placed an additional constraint on the engine selection [1].

Table 8 Propulsion System Requirements

Parameter	Value
Takeoff Thrust [lbf]	81,653
Cruise Thrust [lbf] (M = 0.82, 31,000ft)	14,156

3. Selected Engine

Four General Electric GE90-85B 2-spool high-bypass turbofan engines were selected as the propulsion system of Gravibus. The GE90-85B was originally certified in 1995, satisfying the EIS requirement [15]. The GE90-85B has a 1/3/0/10/2/6 staging arrangement and a bypass ratio of 8.4 [16]. The military jet fuel JP-8 will be used. The reported performance of the engine are given in Table 9 with data taken from an engine database [16].

Table 9 Reported Engine Performance

Parameter	Value
Takeoff Thrust [lbf]	88,870
Cruise Altitude [ft]	35,000
Cruise Mach	0.83
Cruise Thrust [lbf]	17,500
Cruise SFC [lb/lbf-hr]	0.52
Unit Weight [lb]	17,400

Although the reported and required engine performance specify different cruise conditions, the GE90-85B offers sufficient excess thrust than is anticipated to be sufficient at any point in the required flight envelope. However, this must be verified with simulated engine performance. The cruise SFC of 0.52 lb/lbf-hr was used to get preliminary range and fuel weight estimates. This is considered a conservative number because the reported SFC occurs at an engine running at full throttle, while the GE90-85B will be running at partial power during cruise.

B. Engine Modeling

1. Methodology

The GE90-85B was modeled using the turbine engine simulation software GasTurb [17]. The goal of the model is to produce data that resembles data given in the GE90-85B's Type Certification Data Sheet [15]. If the GasTurb model aligns with the reported engine behavior at certain conditions, the values reported by the model at other conditions can be considered accurate as well.

GasTurb receives dozens of parameters regarding flight conditions, engine efficiencies, engine architecture, etc. as inputs. GasTurb also has an iteration feature, where it performs iterations on a specified input until a desired output is reached. Select iterations were conducted in order to bring the model performance close to expected results. Table 10 lists parameters held constant. These values were informed by references [16], [18], and [3]. Table 11 lists iterated input parameters, the target output corresponding to the iteration, and the final value of the input. The input parameters and iterations were aligned with performance of the GE90-85B at its takeoff thrust rating as reported in [15].

Table 10 GasTurb Model Inputs

Input Parameter	Value	Input Parameter	Value
Altitude [ft]	0	Fuel Heating Value [BTU/lb]	18552.4
Mach Number	0	HP Spool Mechanical Efficiency	0.99
DISA [R]	27	LP Spool Mechanical Efficiency	0.99
Intake Pressure Ratio	1	Burner Pressure Ratio	0.95
HPC Pressure Ratio	23	Inner & Outer LPC Polytropic Efficiency	0.93
Bypass Duct Pressure Ratio	0.98	LPC Inlet Mach Number	0.65
Turbine Interduct Reference Pressure Ratio	0.99	HPC Polytropic Efficiency	0.91
Compressor Interduct Pressure Ratio	1	Nominal HP Spool Speed [rpm]	10918
Design Bypass Ratio	8.4	HPT & LPT Polytropic Efficiency	0.93

Table 11 GasTurb Model Iterations

Iteration Input	Converged Input	Target Output	Target Output Value
Inlet Corrected Mass Flow [lb/s]	3052.72	Engine Mass Flow [lb/s]	2976.24
Burner Exit Temperature [F]	2438.38	Net Thrust [lbf]	88,870
Outer Fan Pressure Ratio	1.56894	Ideal Jet Velocity Ratio	0.8
Inner Fan Pressure Ratio	1.7087	Overall Pressure Ratio	39.3
LPC Tip Speed [ft/s]	1322.94	LP Spool Speed [rpm]	2465
LPC Inlet Radius Ratio	0.387	LPC Inlet Tip Diameter [in]	123

2. Model Validation

Table 12 compares the GasTurb model of the GE90-85B to expected performance. It is important to note the differences in how the indicated exhaust gas temperature is taken. In the GE90-85B's type certification data sheet [15], the exhaust gas temperature is "measured at the inlet of the LP Turbine." GasTurb reports the temperatures directly at the end of the burner, and directly after the LP Turbine, and does not account for a temperature gradient between the exit of the burner and the LP Turbine. Therefore the average value and standard deviation between those two temperatures were taken and can be assumed to be analogous to the temperature reported in the Type Certification Data Sheet.

Table 12 GasTurb Model Results

Static Sea-level Takeoff [15]	Model Results	Reported Value	Percent Error
Takeoff Thrust [lbf]	88,870	88,870	0
LP Spool Speed [rpm]	2,465	2,465	0
HP Spool Speed [rpm]	10,918	10,918	0
Indicated Exhaust Gas Temperature [F]	2,013± 425	1,885	6.82
0.83 M, 35,000ft Cruise [16]	**Model Results**	**Reported Value**	**Percent Error**
Thrust [lbf]	16,579	17,500	5.26
SFC [lb/lbf-hr]	0.564	0.5200	8.46
0.82 M, 31,000ft Cruise	**Model Results**	**Requirement**	**Margin of Safety**
Thrust [lbf]	19,175	14,156	35.5%
SFC @ Required Thrust [lb/lbf-hr]	0.497	0.52	4.6%

At the static sea-level takoff condition, the model behaves nearly identically to the GE90-85B as reported. At Mach 0.83, 35,000ft cruise condition, the model under predicts thrust and over predicts SFC, yet remaining within 10% error. The model shows that at the Mach 0.82, 31,000ft cruise condition, the engine meets and exceeds the performance demands from initial sizing. Therefore, since the model remains below 10% error and shows the engine can meet performance demands, full engine maps were generated and data used to perform detailed performance analyses.

3. Model Data

Thrust and SFC as functions of Mach and altitude are able to be calculated from GasTurb, as shown in Figs. 17 and 18. Figure 17 shows engine data at the takeoff operating condition, while Fig. 18 shows engine data at the maximum continuous operating condition.

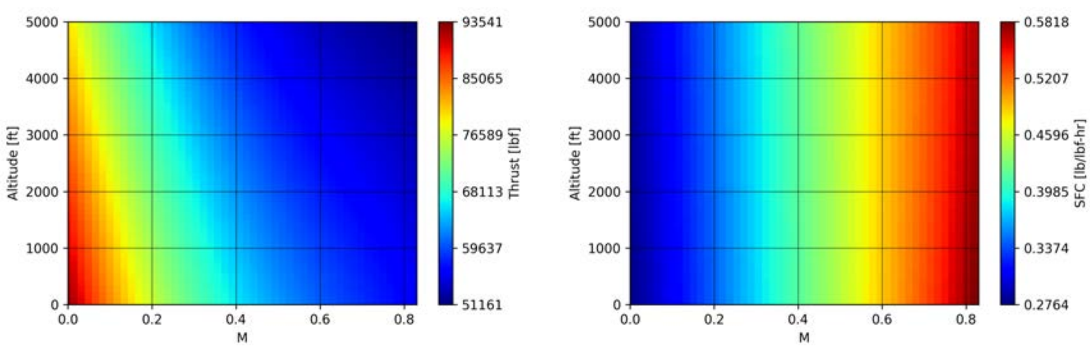

Fig. 17 Full Throttle Takeoff (DISA = 0F)

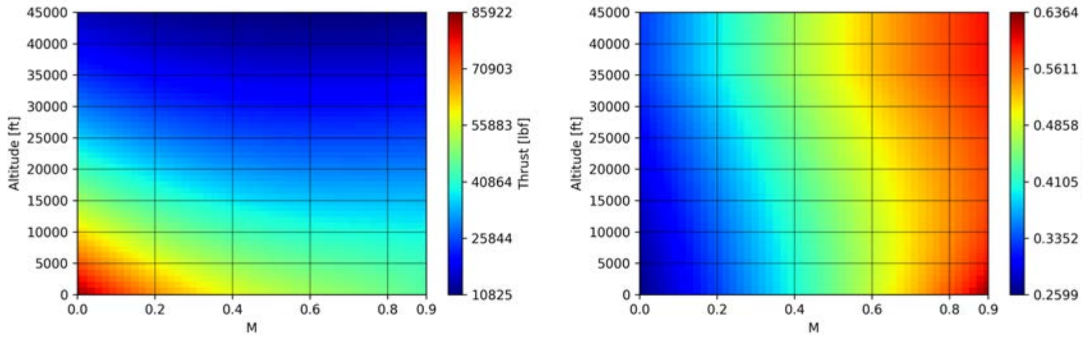

Fig. 18 Full Throttle Max Continuous (DISA = 0F)

The data matches expected trends in thrust and SFC. It can be observed that thrust decreases as Mach number and altitude increase, and that SFC increases with Mach number and altitude. It can also be observed that at identical conditions, the full throttle takeoff thrust is greater that the full throttle max continuous thrust. This matches expectations as in the max continuous operating condition, less fuel is burned and the combustion occurs at a lower temperature than at the takeoff thrust condition.

Figures 19 and 20 show the GE90-85B's cruise SFC as functions of altitude and power at two different Mach numbers. The left plots place net thrust on the x axis, while the right plots show the same data but with part power, or engine throttle, on the x axis. It can be seen that the Gravibus cruises at a condition near the bottom of the SFC curves, limiting fuel consumption to a minimum. At these conditions, the SFC is below 0.5 lb/lbf-hr, meaning that the Gravibus has more efficient fuel burn than the preliminary value of 0.52 lb/lbf-hr.

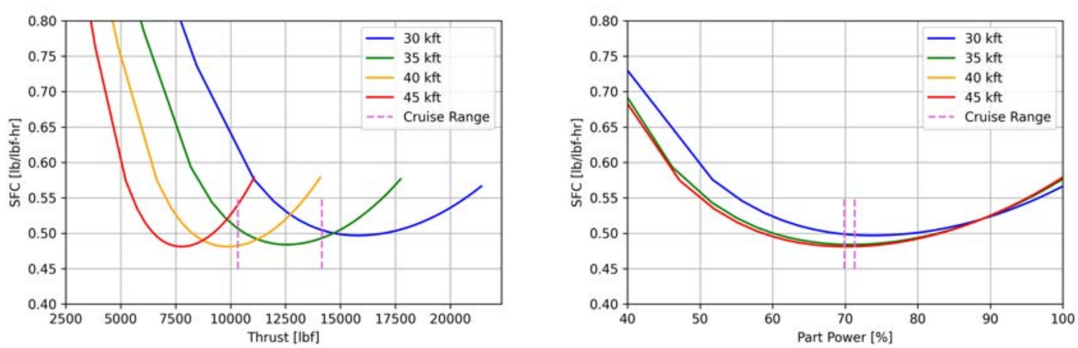

Fig. 19 M = 0.82 Cruise Performance (DISA = 0F)

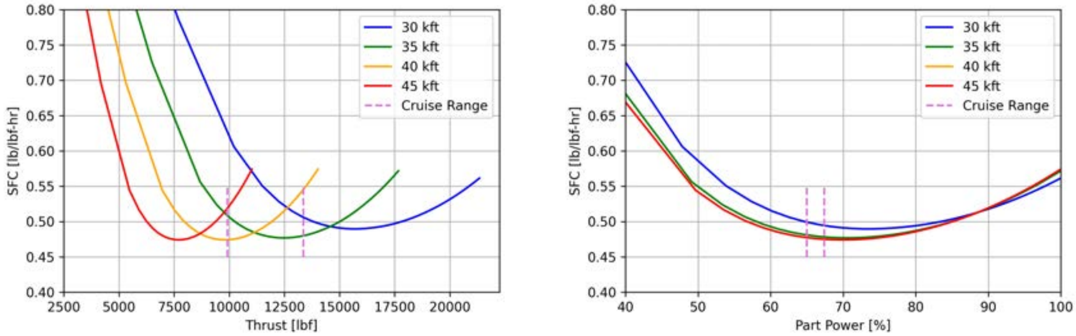

Fig. 20 M = 0.80 Cruise Performance (DISA = 0F)

C. Engine Systems

1. Configuration

A qualitative trade study was performed on the location of the engines. Two configurations were considered: engines mounted underneath the wing, and engines mounted on top of the rear of the fuselage. Both configurations can be seen in Fig. 21.

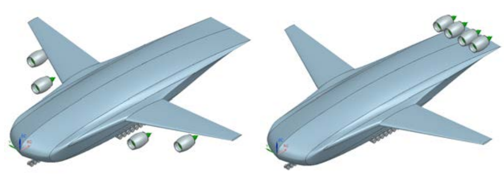

Fig. 21 Candidate Engine Configurations

Rear-mounted engines are the most common configuration seen in other blended wing body concepts and have the advantage that there is less yaw moment induced from an engine out condition. However, rear-mounted engines are subject to the challenge of boundary layer ingestion from the fuselage. Boundary layer ingestion will cause cyclical loading in the engine fan blades, necessitating greater engine weight and/or reducing engine lifespan. At high angles of attack, the flow on top of the fuselage could separate, preventing sufficient mass flow to the engine. Also, engines placed at the rear are mounted high relative to the aircraft's CG, causing a pitch-down moment. Rear-mounted engines also bring the aircraft's CG farther aft. These two effects are adverse to aircraft stability and control. Being on top of the fuselage also makes accessing the engines for maintenance and repair more difficult. Adding sufficient structural supports for the engine within the thin volume of the fuselage trailing edge will also be a challenge and likely cause more structural weight.

Conversely, mounting the engine on the wing comes with several advantages. Due to the large dimensions of the fuselage, there is space to place the engines beneath the wing and have an abundance of clearance from the ground. Underneath the wings, the engines are closer to the CG and will impart far less pitching moment, a favorable outcome for stability and control. Engines beneath the wing do not inject boundary layers, so the fan blades will not see cyclical loading. Therefore, wing-mounted engines are beneficial to the service life of the engine components. Wing-mounted engines are more accessible for repair and maintenance than rear-mounted engines. Wing-mounted engines reduce the structural weight of the wings as they help lower the bending moment at the wing root, a similar effect to placing fuel in the wings. One disadvantage of wing-mounted engines is that in an engine out condition, a larger yaw moment is induced, requiring a larger vertical stabilizer. Table 13 summarizes the advantages and disadvantages of each configuration. Since it was favorable across most design considerations, the wing-mounted engine configuration was selected for Gravibus.

Table 13 Engine Location Trade Study

Design Consideration	Wing Mounted Engines	Rear Mounted Engines
Engine Out	Unfavorable	Favorable
Aircraft Stability	Favorable	Unfavorable
Structural Weight	Favorable	Unfavorable
Boundary Layer Interaction	Favorable	Unfavorable
Repair and Maintenance	Favorable	Unfavorable

2. Nacelle Design

A nacelle was designed to house the GE90-85B. The inlet area was designed according to methods specificed in Chapter 10 of Raymer [3]. The core and bypass exhaust areas were designed to match exit areas that the GasTurb model reported. Figure 22 illustrates the nacelles dimensions in inches.

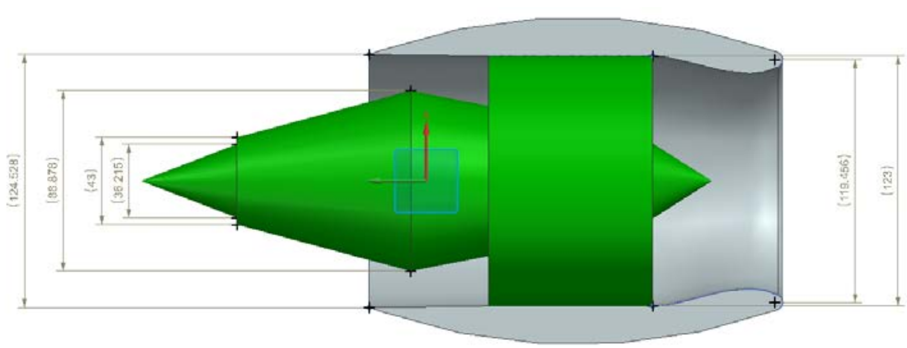

Fig. 22 Nacelle Dimensions

3. Systems Integration

In addition to generating thrust, the four GE90-85B engines will also be supplying power to other systems aboard Gravibus. Gravibus requires 102HP per engine for powering hydraulic pumps, and 150HP per engine for electrical generation. Each GE90-85B comes with three drive pads for powering separate systems. Table 14 details the power capabilities the various drive pads.

Table 14 GE90-85B Accessory Drives

Drive Pad	System Type	Rated Horsepower [HP]
IDG	Electrical	243
Hydraulic Pump	Hydraulic	85
VSCF/PMG Generator	Electrical	58

In order to satisfy Gravibus' system power requirements, each engine will cover the 150HP electrical demand using the IDG drive pad, and the 85HP from the hydraulic pump as well as some remaining HP from the IDG to satisfy the 102HP hydraulic demand. The engines will also be supplying compressed bleed air to the ECS to maintain cabin/cargo bay pressure. Figure 23 shows a diagram of the integrated engine system architecture.

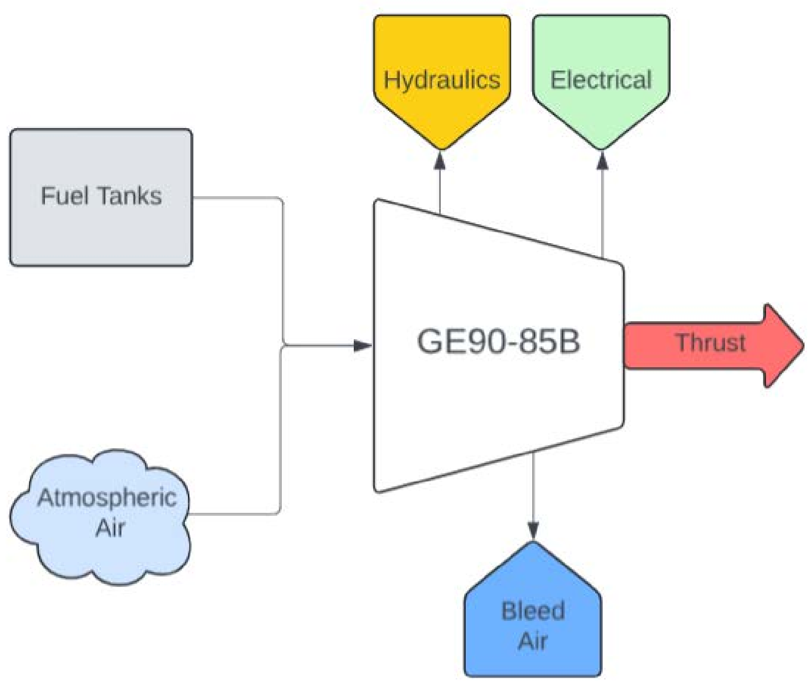

Fig. 23 Propulsive System Architecture

VI. Performance

A. Takeoff and Landing Performance

Gravibus must be able to meet a BFL of 9,000 ft by 150 ft at sea level (h_p = 0ft) and $\Delta ISA = 15°C$ [1]. This BFL requirement will also be used as the constraint for the TOFL and LFL. This assumes that if the Gravibus takes off from a 9,000 ft long runway, it must be able to land on the same runway. This requirement must be met on a variety of different runway materials, such as dry, wet, or icy concrete and asphalt. It is unlikely that the Gravibus will takeoff from soft turf or wet grass, as asphalt is the most desirable runway material to withstand large amounts of weight. In addition, the RFP states that the HLA will not be deployed to unprepared runways. Therefore, these runway materials will not be considered. Respective TOGWs and fuel weights required for each mission, shown in Table 15 will be used to analyse take-off and landing. These values were determined by iterating the required fuel weight for each mission separately until 99% of fuel was used. C_L takeoff was set to 2 and C_L landing was calculated to be 2.119. A value of 2 was chosen so as to maximise ROC and minimize drag during takeoff. Reserves were set to 10% of total fuel burned, which satisfies MIL-STD-3013 [2] and at an altitude of 10,000 ft.

Table 15 TOGWs and Fuel Weights Required

Mission	TOGW (lbs)	Fuel Required (lbs)
Maximum Payload Mission	1,117,941	212,000
Mid Payload Mission	1,160,241	389,300
Ferry Mission	703,441	227,500

Runway material coefficients from Table 16 are used to determine the TOFL, LFL and BFL [3]. An obstacle height of 50 ft was used based on MIL-STD-3013 [2]. As seen in the values reported in Table 16, Gravibus is able to meet the BFL requirement for all runway materials, for all three missions. The Gravibus is unable to meet LFL requirements for icy concrete for the maximum and mid payload missions. However, it meets the LFL requirement for the ferry mission on icy concrete. Due to the nature of long flight time's for the ferry mission, weather conditions can often be unpredictable. The capability of the Gravibus to land on icy concrete within the runway requirement, means that the aircraft itself can be transported in any weather condition for long distances.

Table 16 TOFL and LFL Distance Performance

	Conditions		Max Payload Mission			Mid Payload Mission			Ferry Mission		
Surface	μ	μ_b	TOFL (ft)	LFL (ft)	BFL (ft)	TOFL (ft)	LFL (ft)	BFL (ft)	TOFL (ft)	LFL (ft)	BFL (ft)
Dry concrete/asphalt	0.04	0.3	7,860	8,790	7,860	8,550	7,700	8,550	3,180	6,010	3,180
Wet concrete/asphalt	0.05	0.225	8,010	8,760	8,010	8,720	7,670	8,720	3,200	5,790	3,200
Icy concrete/asphalt	0.02	0.08	7,590	13,660	7,590	8,230	11,940	8,230	3,130	8,420	3,130

B. Mission Segment Performance Analysis

A performance analysis tool was created involving altitude-step integration for climb and descent, and range-step integration for cruise. The cruise segment employs range-step to ensure the Gravibus meets the RFP range requirement for each mission, as the RFP also states that the range cannot include climb and descent. This tool calculates significant atmospheric, aerodynamic and propulsion values, and weights at every step of the mission. The climb, cruise, and descent segments were calculated separate from the takeoff and landing analysis. A TOC of 31,000 ft for the max and mid payload missions was chosen, and a TOC of 32,000 ft was selected for the ferry mission. These values were determined by an in-depth trade study that will be discussed in Section VI.F.

1. Maximum Payload Mission

The maximum payload mission requires the Gravibus to carry a payload of 430,000 lbs and meet a cruise range of 2,500 nmi. The mission profile in 3 provides a visual depiction of the mission. The fuel required for each segment is shown in Table 17.

Table 17 Segment Fuel Burn Summary for Max Payload Mission

Segment	Fuel Burn (lbs)	Fuel Fraction (%)
WUTTO	2,475	1.16
Climb	13,475	6.36
Cruise	165,545	78.09
Descent	9,835	4.64
Reserves/Loiter	19,135	9.03

The drag values for each flight segment are shown in Table 18. The values reported in the table were calculated by taking the average of each parameter over each flight segment. As expected, the the drag values decrease as fuel is burned and the weight of the aircraft lowers as the mission progresses.

Table 18 Segment Drag Summary for Max Payload Mission

Segment	C_D	$\frac{L}{D}$	Drag (lbs)
WUTTO	0.1573	9.873	112,987
Climb	0.0286	17.665	62,775
Cruise	0.0336	18.427	55,298
Descent	0.0330	18.355	50,892
Reserves/Loiter	0.0321	18.409	50,500

2. Mid Payload Mission

The mid payload mission consists of a payload of 295,000 lbs for a cruise range of 5,000 nmi. The fuel burn segments for this mission are shown in Table 19. This mission requires the most amount of fuel as the Gravibus must fly for a larger range than the max payload mission, and with a heavy payload.

Table 19 Segment Fuel Burn Summary for Mid Payload Mission

Segment	Fuel Burn (lbs)	Fuel Fraction (%)
WUTTO	4,545	1.16
Climb	15,135	3.89
Cruise	324,545	83.37
Descent	9,665	2.48
Reserves/Loiter	35,390	9.09

The drag values for each flight segment for the mid payload mission are shown in Table 20. The values reported in the table were calculated by taking the average of each parameter over each flight segment. As expected, the the drag values decrease as fuel is burned and the weight of the aircraft lowers as the mission progresses, similar to the max payload mission.

Table 20 Segment Drag Summary for Mid Payload Mission

Segment	C_D	$\frac{L}{D}$	Drag (lbs)
WUTTO	0.2684	7.452	155,079
Climb	0.0367	18.318	62,698
Cruise	0.0326	18.306	53,106
Descent	0.0301	17.942	45,319
Reserves/Loiter	0.0292	17.982	44,991

3. Ferry Mission

The ferry mission consists of no payload for a cruise range of 8,000 nmi. This is the largest range the Gravibus is required to make. The fuel burn segments for this mission are shown in Table 21. This mission requires the least amount of fuel as it weighs the lightest.

Table 21 Segment Fuel Burn Summary for Ferry Mission

Segment	Fuel Burn (lbs)	Fuel Fraction (%)
WUTTO	2,655	1.16
Climb	10,180	4.47
Cruise	187,040	82.22
Descent	6,450	2.84
Reserves/Loiter	20,635	9.07

The drag values for each flight segment for the ferry mission are shown in Table 22. The values reported in the table were calculated by taking the average of each parameter over each flight segment. This mission has the lowest drag value for WUTTO as it has the lightest TOGW.

Table 22 Segment Drag Summary for Ferry Mission

Segment	C_D	$\frac{L}{D}$	Drag (lbs)
WUTTO	0.3496	5.720	122,513
Climb	0.0259	19.594	35,569
Cruise	0.0199	19.665	27,574
Descent	0.0300	13.323	37,564
Reserves/Loiter	0.03002	13.323	37,448

C. Aircraft Performance Coefficients

The performance analysis tool is also used to determine the maximum aircraft coefficient $\frac{C_L}{C_D}$. This is done by taking the calculated values of C_D and the chosen climb C_L values at the TOC altitude and cruise Mach, to calculate $\frac{L}{D}$. The values are shown in Table 23.

Table 23 Maximum Aircraft Performance Coefficients

Maximum Payload Mission				Mid Payload Mission				Ferry Mission			
Altitude	Mach Number	CL	L/D	Altitude	Mach Number	CL	L/D	Altitude	Mach Number	CL	L/D
31,000	0.82	0.61	18.36	31,000	0.82	0.67	18.33	32,000	0.82	0.425	19.92

D. Payload-Range Diagram

A payload diagram, shown in Fig. 24, confirms that Gravibus is able to carry the payload required for each mission, and meet the range requirements. Points A to B represent a trade of payload for range while maintaining the maximum takeoff weight limit and illustrate that the aircraft is capable of carrying 430,000lbs over a range of 2,500 nmi. Point C represents the aircraft carrying the mid payload of 295,000 lbs and meeting the range requirement of 5,000 nmi. Finally, Point D shows the ferry mission, with no payload, reaching a required range of 8,000 nmi.

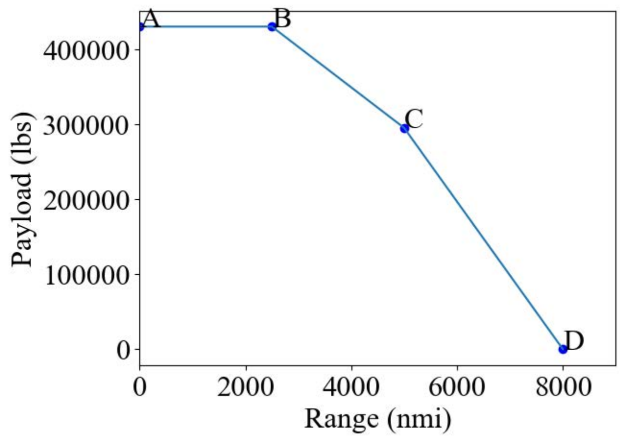

Fig. 24 Payload-Range Diagram

E. Flight Envelope Diagram

The full flight envelope for the Gravibus is shown in Fig. 25 and shows the safe operating region for the aircraft. The limits of this flight envelope consist of the stall speed, Q limit, absolute ceiling and maximum Mach number. The absolute ceiling of the Gravibus is 45,900 ft, while the service ceiling is 45,400 ft.

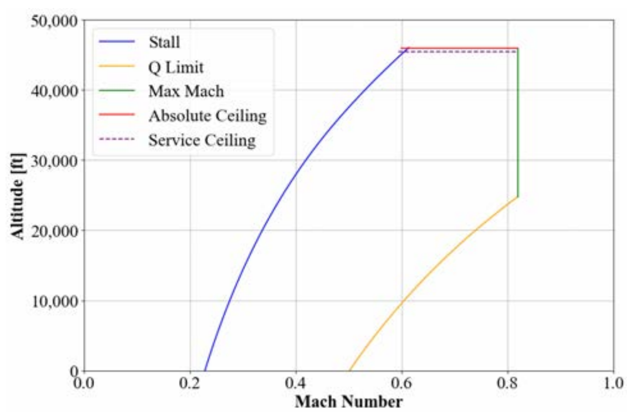

Fig. 25 Flight Envelope Diagram

F. Trade Study: Top of Climb

A trade study was conducted to determine the optimal TOC for each mission, to increase fuel efficiency. This was done by taking the performance analysis tool and simulating each mission to reach a variety of different TOCs from 31,000 ft to 34,000 ft. These values were chosen as the Gravibus' altitude continues to increase during cruise, and cannot exceed 43,000ft, as per RFP requirements. The total fuel required was summed at the end of each simulation to determine what altitude would be most optimal to start the cruise segment at. Figure 26 shows the amount of fuel required for each mission at each TOC, as a percentage of the minimum amount of fuel possible. It was established that for the max and mid payload missions, a TOC of 31,000ft would be required to burn the least amount of fuel. It was also determined that for the ferry mission, a TOC of 32,000ft was most ideal when compared to 31,000 ft, 33,000 ft, and 34,000 ft. This resulted in a decrease of fuel burned of 1,500 lbs from initial fuel estimates. This final fuel amount was used in takeoff, landing and mission simulations in Sections VI.A and VI.B.

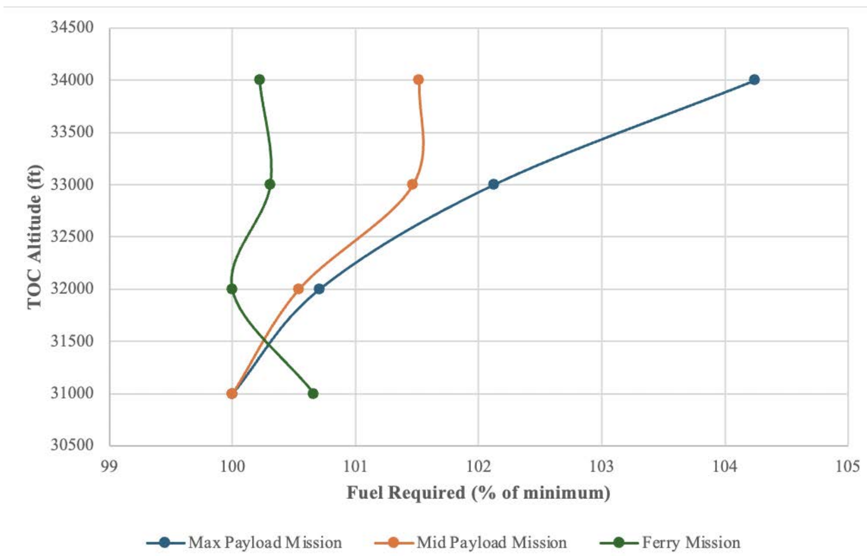

Fig. 26 TOC vs. Fuel Required

VII. Aerodynamics

A. Methodology of Aerodynamic Design

Computational fluid dynamics (CFD) was the main tool used in the aerodynamic analysis of Gravibus due to its novel configuration and lack of empirical data for similarity analysis. Flightstream is a 3-D panel vortex flow solver which provides results of the same level of accuracy as other panel method software in a fraction of time. This tool was utilized in the aerodynamic analysis of Gravibus since it was validated extensively using experimental data. Additionally, Flightsream provides robust results within the transonic regime [19].

During preliminary design, Gravibus underwent a significant iterative design process in order to maximize performance during cruise. Wing planform area, taper ratio, wing twist and the transition space configuration were determined based on multiple trade studies that were conducted in order to minimize CD_i and CD_o. The iterative loop consisted of conducting cruise analysis using Flightstream, making minor configuration modifications based on the previous results, then analyzing the new configuration. This loop continued until range requirements were met for all missions. As a result of the iterative process, the wing section planform area decreased with respect to the reference area defined during initial sizing. Wing twist was chosen also to delay tip stall from occurring by reducing the angle of attack that the tip sees. There is 0 ° twist at the root, and 0 ° twist at the tip. Table 24 outlines the outer wing geometric dimensions. This iterative process ultimately resulted in Gravibus improving in cruise performance by decreasing drag and becoming a more aerodynamic body.

Table 24 Wing Section Dimensions

Parameter	Value	Parameter	Value
Wing Area [ft^2]	5,314	MAC [ft]	28
Total Aircraft Span [ft]	262	Root Chord [ft]	39.5
Wing Section Span [ft]	207	Tip Chord [ft]	11.48
AR	8.1	Taper Ratio [ft]	0.3
$C/4$ Sweep [deg]	25	Twist [deg]	0-2

Several wing parameters were determined from initial sizing. These include reference area, span, and the tip and root chords. Wing sweep was initially selected from similarity analysis using the C-5A [20]. Since Gravibus cruises at a higher Mach number than the C-5, a wing sweep trade study was conducted to investigate whether increasing sweep provided sufficient wave drag reduction. This trade study was coupled with an airfoil thickness trade study which is discussed in Section VII.B. Using the delta method, it was found that increasing sweep by 4° only reduced wing wave drag by at most 3 counts [21] for every $\frac{t}{c}$ investigated. Due to diminishing returns and in order to reduce structural weight, it was decided that no further sweep above 25° was needed. Table 25 tabulates wave drag for different $\frac{t}{c}$ and sweeps.

Table 25 Wing Section Wave Drag, in Counts

	t/c 10%	t/c 12%	t/c 14%
25°c/4 Sweep	4	6	14
27°c/4 Sweep	3	5	12
29°c/4 Sweep	2	4	11

B. Wing and Body Airfoil Selection

One main driver of airfoil selection for Gravibus was the minimization of wave drag that occurs due to the formation of shocks over the top of the wing and body. Shocks are expected to form on top of Gravibus as it cruises at Mach 0.8. Supercritical airfoils reduce wave drag by pressure recovery and weakening the normal shock strength. For these reasons, airfoil selection was narrowed down to supercritical airfoils for both the wing section and main body. The NASA Supercritical Series is a family of supercritical airfoils with wide ranges of design C_L and thickness ratios, $\frac{t}{c}$. This allows for flexibility in choosing an airfoil based on the design point of Gravibus. This airfoil family, as well as the DFVLR R-4 and RAE 5215, were considered for selection. For the NASA Supercritical Series, design C_L of 0.4 and 0.6 were investigated since this is the minimum and maximum C_L Gravibus experiences during cruise, respectively. For wing airfoil thickness, a 10-14% range was investigated based on similarity analysis and historical trends provided in Chapter 4 in Raymer [3]. For the main body, it was determined that a minimum $\frac{t}{c}$ of 12% was needed due to volumetric constrains of the pressure vessel. During the iterative design process, it was concluded that a symmetrical airfoil was needed for the main body in order to minimize both CD_i and CD_o of the entire aircraft.

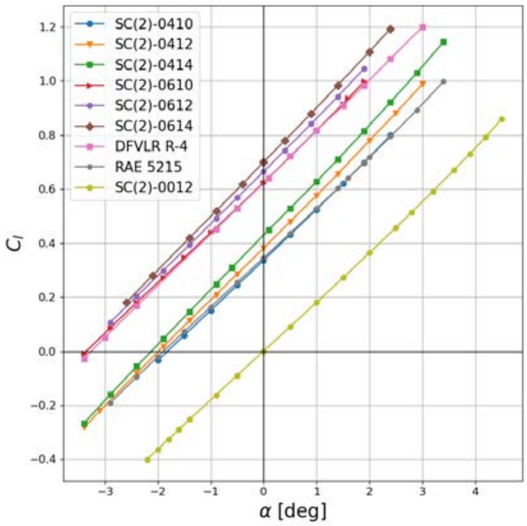

(a) Airfoil Lift Curve Slope

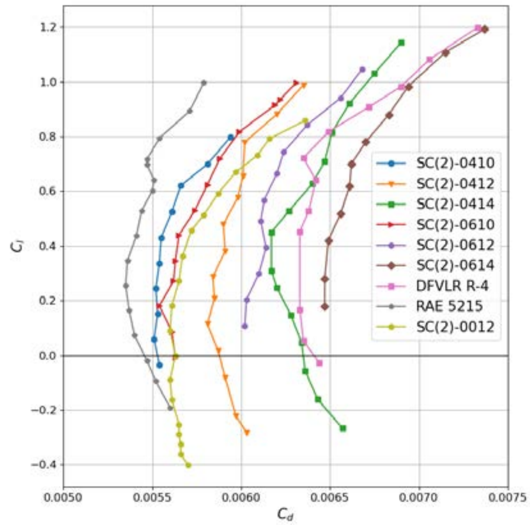

(b) Airfoil Drag Polar

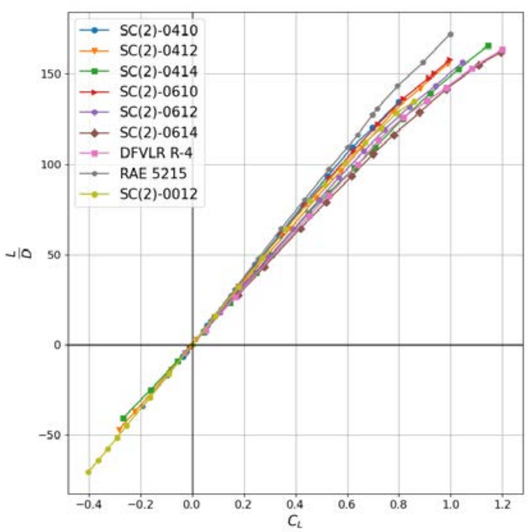

(c) Airfoil Lift-to-Drag vs. Lift

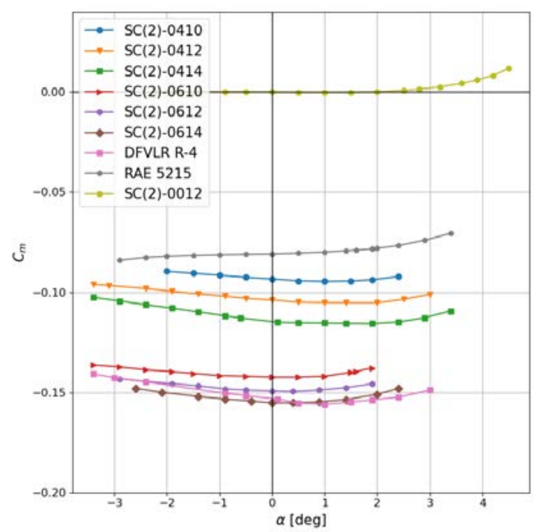

(d) Airfoil Moment Coefficient Curve

Fig. 27 Viscous Airfoil Analysis at Re = 62e10 and Mach = 0.7 using XFOIL.

Xfoil is a higher-order 2-D panel method and was used for airfoil analysis. Since it does not predict shocks, accurate results at a cruise Mach of 0.8 cannot be obtained using this software. However, this tool is still useful to quickly analyze general airfoil performance for Mach numbers below the critical Mach number. Viscous analysis was done at the wing Reynold's number of Re=62e6 and a Mach of 0.7, which is just below the lowest critical Mach number of all the airfoils investigated. The results are shown in Fig.27. Airfoils of the same design C_l but different thicknesses do not vary significantly in performance, specifically in L/D. This allows for other characteristics, specifically thickness and design C_l to be the main drivers in airfoil selection for Gravibus.

For the wing section, a trade study tabulated in Table 25 was conducted to determine the appropriate $\frac{t}{c}$. It was found that wave drag for a 14% thick airfoil is roughly double that of a 12% thick airfoil. While a 10% thick airfoil produces the least wave drag, it was decided that a 12% thick airfoil would be used for Gravibus in order to provide enough room for systems and to increase structural efficiency. During the iterative design process, it was found that an airfoil of 0.6 design C_l at the root and 0.4 design C_l at the tip provided the best L/D for cruise. Therefore, it was concluded that the SC(2)-0612 and SC(2)-0412 airfoils would be used for the wing root and wing tip sections on Gravibus, respectively. Additonally, due to its low lift and low moment characteristics, it was determined that the SC(2)-0012 airfoil was best suited for the main body. Plots of the body, wing root, and wing tip airfoils are shown in Fig. 28 .

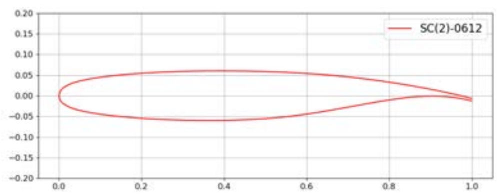

(a) Wing Root Airfoil Section

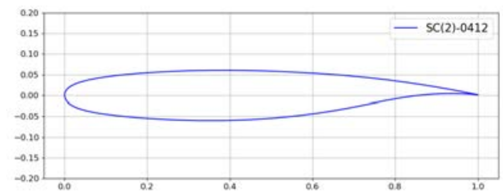

(b) Wing Tip Airfoil Section

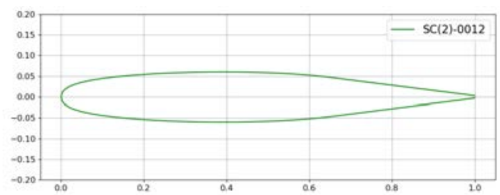

(c) Main Body Airfoil

Fig. 28 Gravibus Airfoil Sections

C. High-Lift System

The high-lift system for Gravibus was designed based on similarity analysis and performance requirements to meet a takeoff and landing C_L of 2.0 and 2.12. Gravibus contains a full-span leading edge slat and a trailing edge Fowler flap, which are the same high-lift devices used on the C-5A [20]. It was determined from performance that this system satisfies the required additional lift needed to meet takeoff and landing, therefore no further changes in device type or span was needed. Flightstream was not able to predict stall for Gravibus, due to the overprediction of lift. Maximum clean lift for the wing section section was estimated using Equation (12.15) in Raymer. Additional lift values for takeoff and landing were estimated using methods specified in Chapter 12 in Raymer [3]. Important high-lift device characteristics are summarized in Table 26. The integration of the high-lift devices within the wing section are seen in Fig. 30. The wing planform with dimensions are shown in Fig. 29.

Table 26 Change in Maximum Lift for Each High-Lift Device

High-Lift-Device	Span from root chord [ft]	cf/c	$S_{flapped}/S_{ref}$	Takeoff ΔC_L	Landing ΔC_L
LE Slat	98.22	0.14	0.96	0.20	0.33
TE Fowler Flap	70.43	0.28	0.85	0.62	1.04

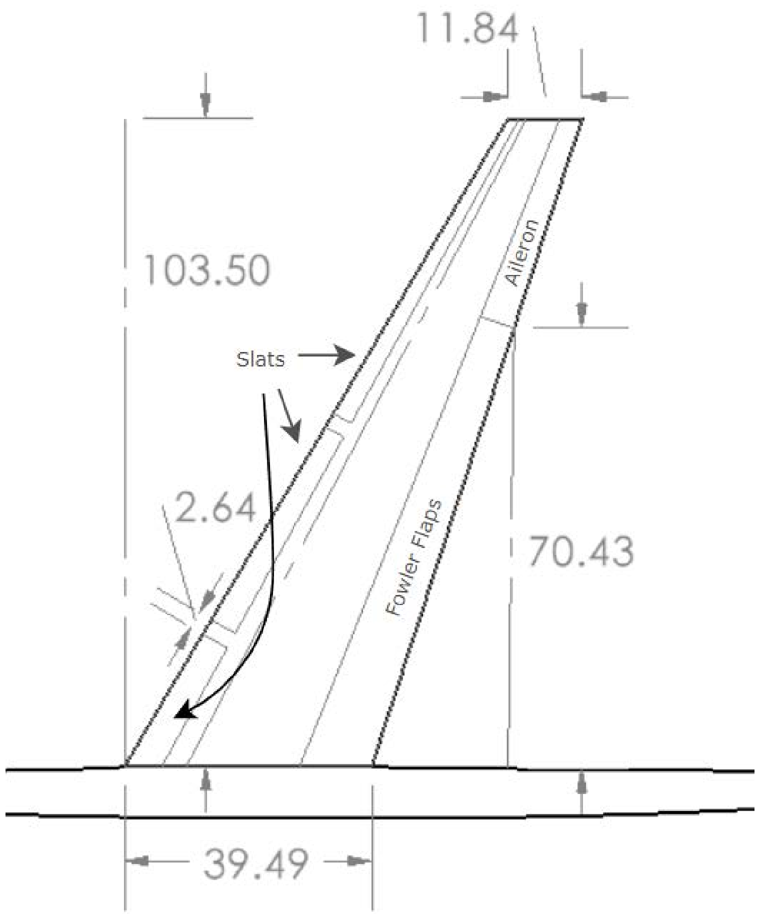

Fig. 29 CAD Drawing of Wing Section With Dimensions in Feet

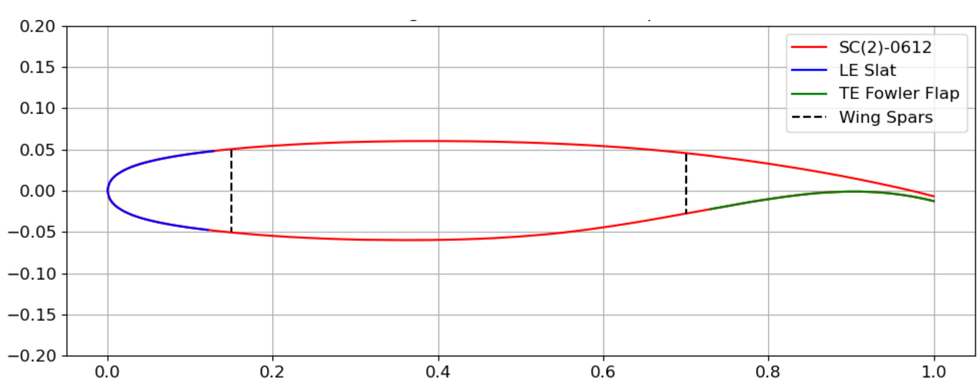

Fig. 30 Cross-section View of High-Lift System

D. Drag Buildup

Drag buildup for Gravibus consists of a combination of Flightstream results and emperical methods from Raymer Chapter 12 [3]. To validate the results obtained from Flightstream, the Raymer component method was used to estimate parasite drag for the nacelle, empennage, and wing. These individual components were then meshed and analyzed seperately in Flightstream. The results are compared and shown in Table 27. It can be seen that the values predicted by Flightstream are reasonably close to that of Raymer. Therefore, it was determined that Flightstream can provide robust drag predictions and can be used to find parasite and induced drag for Gravibus.

While Flightstream provides robust results for the transonic regime, it cannot simulate shocks. Whole aircraft cruise parasite and induced drag were predicted in Flightstream for a Mach number of 0.78 to reduce the presence of sonic flow over the body. This allows for the minimization of inaccurate results due to sonic flow while maintaining a Mach number close to the cruise Mach. All cruise drag values and their respective methods are summarized in Table 28. Extra drag contributions during takeoff and landing were calculated using methods in Raymer Chapter 12 and are tabulated in Table 29 [3]. Typical trailing edge flap deflection angles of 20° and 40 ° were used to estimate the extra drag for takeoff, and landing, respectively.

Table 27 Raymer Component Subsonic Parasite Drag Buildup vs. Flightstream, in Counts

Part	Re [1e6]	C_f	FF	Q	S_{wet}/S_{ref}	CD_o (Raymer)	CD_o (Flightstream)
Wing Section	62	0.002	1.5	1.0	1.82	50	48
Vertical Tail	7.8	0.003	1.1	1.05	0.43	15	11
Horizontal Tail	15.5	0.003	1.1	1.05	0.85	26	22
Nacelle	52.7	0.002	1.28	1.3	0.21	30	35

Table 28 Cruise Drag Totals

Drag Type	C_{D_o}	C_{D_i}	$C_{D_{trim}}$	$C_{D_{wave}}$	$C_{D_{L+P}}$	C_D
Value	0.022	0.003	0.0017	0.001	0.0006	0.028
Method	CFD	CFD	Raymer	Delta Method	Raymer	

Table 29 Extra Drag Contribution Due to High-Lift Devices

Drag Type	**Takeoff**	**Landing**
ΔC_{D_o}	0.021	0.059
ΔC_{D_i}	0.022	0.062
ΔC_D	0.043	0.12

E. Aircraft Aerodynamic Performance

Important aircraft aerodynamic curves for cruise, takeoff and landing are shown in Fig. 31. All curves were constructed using Flightstream at their respective freestream conditions. Each curve was constructed using discrete data points rather than a smooth function. The cruise design point as well as required takeoff and landing C_L values are marked in each appropriate graph. Major aircraft aerodynamic properties are tabulated in Table 30. While the wetted area of Gravius is high relative to historical trends, it performs higher than most millitary aircraft when looking at the max L/D vs wetted aspect ratio trends in Raymer Chapter 3 [3].

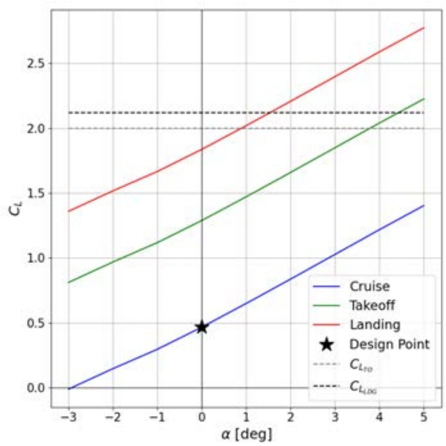

(a) Gravibus Lift Curve

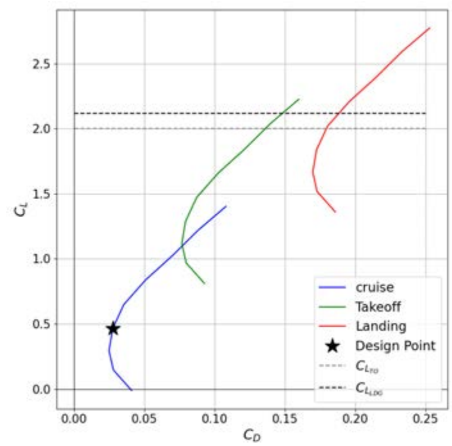

(b) Gravibus Drag Polar

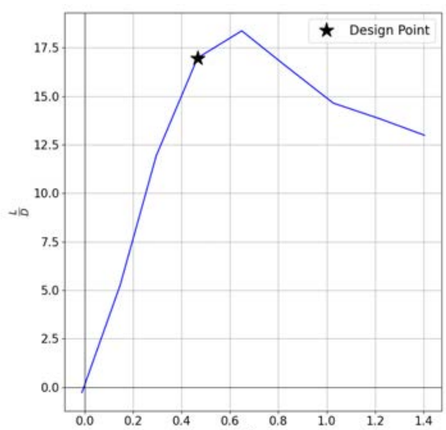

(c) Gravibus L/D vs. Lift

Fig. 31 Gravibus Aerodynamic Performance During Cruise

Table 30 Major Aircraft Parameters

Parameter	Cruise C_L	Cruise C_D	L/D Cruise	Cruise α	TO C_L	Landing C_L	Wetted-to-Reference Area
Value	0.47	0.028	17.4	0 °	2.0	2.12	8.2

VIII. Stability and Control

A. Stability Derivatives

The Athena Vortex Lattice software (AVL) was the primary source for obtaining the stability derivatives. These values were crucial in the sizing and implementation of the control surfaces, and are summarized in Table 31. The conditions for takeoff, cruising, and landing were used in order to obtain an idea of the sizing and required deflection. Cm_α was negative for each condition tested, which confirms that the Gravibus is statically stable in the longitudinal direction. The CFD results were verified by performing hand calculations as prescribed in Nelson [22].

Table 31 Stability Derivatives

Conditions	CL_α [rad^{-1}]	Cm_α [rad^{-1}]	$Cm_{\delta e}$ [rad^{-1}]	ϵ_α [rad^{-1}]	Cl_β [rad^{-1}]	Cn_β [rad^{-1}]
Takeoff	4.45	-1.23	-1.92	0.183	-0.075	0.091
Cruise	6.09	-1.44	-2.81	0.25	-0.051	0.084
Landing	4.63	-1.31	-1.84	0.19	-0.008	0.070

The static margin was calculated through using the neutral points at different flight conditions. The criteria for stability was to have the stability margin above 5% in order to determine that the aircraft is indeed statically stable in the longitudinal direction. Table 32 displays what the static margins are for each flight condition.

Table 32 Static Margin and Neutral Point for Various Flight Conditions

Conditions	Takeoff	Cruise	Landing
Static Margin [%]	27.60	23.67	28.29
Neutral Point [% MAC]	34.4	34.4	34.4

B. Empennage

The sizing process for the horizontal and vertical tails began with collecting data on other aircraft of the same class. Tail volume coefficients from empirical sources, such as Raymer, as well as published data were used [3, 23] and are summarized in Table 33.

Table 33 Tail Volume Coefficients and Area Ratios

Parameter	Raymer	Boeing 777	Airbus A321	Ilyushin Il-86
C_{HT}	1.0	0.891	0.957	0.935
C_{VT}	0.09	0.065	0.079	0.092
S_h/S_w	-	0.237	0.253	0.284
S_v/S_w	-	0.124	0.176	0.178

1. Horizontal Tail

While the tail volume coefficient served as a starting point for the horizontal tail, the scissor-notch diagram was critical in determining the final sizing. The scissor-notch diagram can be seen in Fig. 32. The method for the creation of the diagram were derived from Torenbeek[24].

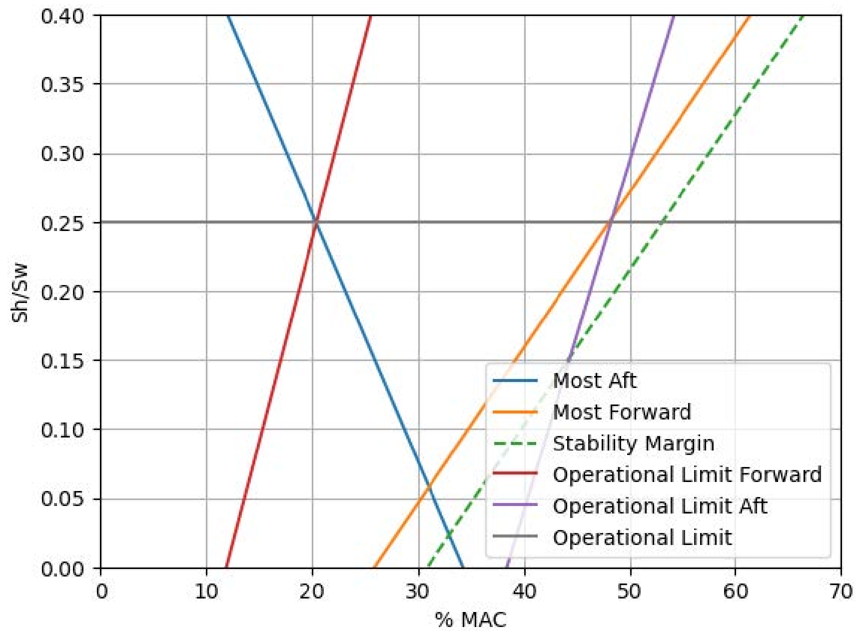

Fig. 32 Scissor-Notch Diagram

As seen from Fig. 32, the most optimized ratio for S_h/S_w is about 0.25, which aligns well with the values of other heavy-lift aircraft, as most values fall between 0.225 and 0.30. Thus, the horizontal tail was sized accordingly, and its main parameters are summarized in Table 34.

Table 34 Geometric Parameters of the Horizontal Tail

Geometric Parameters	Horizontal tail
S_h/S_w	0.25
Area	1,500 sq ft
Span	77 ft 5.4 in
AR	4.0
λ	0.4
c/4 Sweep	30 °
X_{LE}	125 ft
C_{HT}	0.94
Airfoil	NACA 0009

2. *Vertical Tail*

A trade study was conducted in determining the benefits and drawback of having a singular vertical tail rather than the twin tail configuration. The two configurations were tested in AVL to see the different in control and stability derivatives in order to see how each configuration performed against one another. The results can be seen in Table 35.

Table 35 Difference in Control Derivatives between Vertical Tail configuration

Control/Stability Derivatives	Twin Tail	Singular Tail
Cn_β	0.0927	0.171
CY_β	-0.247	-0.457
Cn_r	-0.0734	-0.147
CY_r	0.1715	0.373

Although the singular tail would produce more side force and yawing moment with respect to the yaw rate, this aspect would come at the cost of structural weight of the aircraft. The twin tail design, although producing smaller stability/control derivatives, is effective enough for the aircraft's requirements while also providing a more structurally sound design.

As for the selection for airfoil, it was decided that the root and tip airfoils will be NACA 0015 and NACA 0009, respectively. Symmetric airfoils are ideal for stabilizers, and these thicknesses are a compromise between additional control and structures. The key geometric parameters for the vertical tail are summarized in Table 36.

Table 36 Geometric Parameters and Sizing for the Vertical Tail

Geometric Parameters	Vertical tail
S_h/S_w	0.168
Area	1,010 sq ft
Span	46 ft (total)
AR	1.92
λ	0.5
c/4 Sweep	16 °
X_{LE}	125 ft
C_{HT}	0.08
Airfoil	NACA 0015 (Root) NACA 0009 (Tip)

C. Control Surfaces

The control surfaces were primarily sized through the empirical methods in Raymer as well as analyzing other heavy lift aircraft in order to validate the design choices [3, 23]. The deflection ranges has also been verify to meet all requirements. The geometric parameters for all control surfaces are summarized in Table 37 and dimensioned diagrams are shown in Fig. 33.

Table 37 Geometric Parameters of Control Surfaces

Parameter	Elevator	Rudder	Ailerons
Chord [ft]	3.9	5.04	9.63
Span [ft]	27.24	20.25	31.67 ft
Deflection [°]	± 25	± 20	± 15

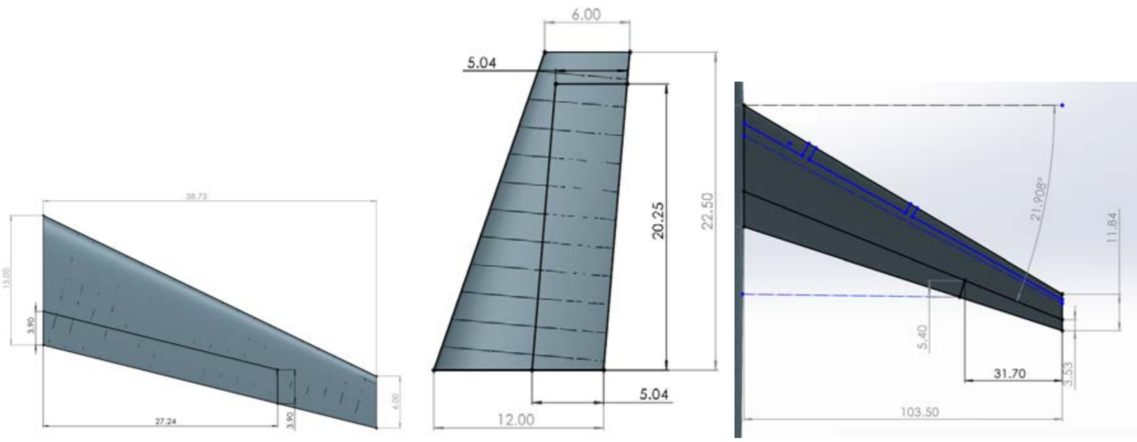

(a) Horizontal Stabilizer **(b) Vertical Stabilizer** **(c) Main Wing**

Fig. 33 Control Surface Geometry

D. Trim Analysis

Trim analysis was conducted through using methods from both Nelson [22] and Raymer [3]. The incidence of the wing was kept at a range between 0 to 2 degrees for the wing and -2 to 0 degrees in the aft. This range was to ensure minimal manual input from the pilot when taking off or landing. The objective is to produce no pitching moment at a given C_L for each condition. The trim diagrams are shown in Fig. 34 and the required deflection for each condition is shown in Table 38.

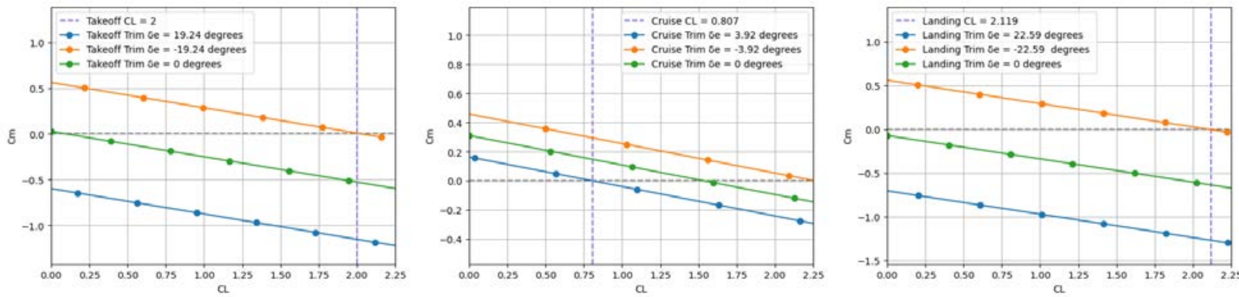

(a) Takeoff **(b) Cruise** **(c) Landing**

Fig. 34 Trim Diagrams

Table 38 Trim Deflection Requirements

	Takeoff	Cruise	Landing
δ_e [°]	-19.24	3.92	-22.39

E. Dynamic Stability

Through the use of AVL, values for Cn_β and and Cl_β were obtained adn can be found in Table 39, and the aircraft was determined to be laterally and directionally static stable. With Cn_β being positive and Cl_β being negative, the aircraft is statically stable in the lateral direction. With these values, dynamic stability can be derived. For obtaining the dynamic stability derivatives, the equations in Nelson [22] were used throughout the calculations. All of these values were found in cruise conditions and are summarized in Tables 40 and 41.

Table 39 Lateral-Directional Stability Derivatives

Cn_β	Cl_β
0.2027	-0.0516

Table 40 Dynamic Stability for Longitudinal Direction

Dynamic Mode	Roots	ω_n	ζ	T_P	$T_{1/2}$
Phugoid	-0.0012 ± 0.0647i	0.064 Hz	0.019	97.112 s	575 s
Short	-0.311 ± 1.053i	1.098 Hz	0.283	5.962 s	2.218 s

Table 41 Dynamic Stability for Lateral Direction

Dynamic Mode	Roots	ω_n	ζ	T_P	$T_{1/2}$	τ	T_2
Roll	-1.95	1.39 Hz	-	-	0.493 s	0.510 s	-
Spiral	-0.015	-	-	-	-	-	46.0 s
Dutch Roll	-0.429 ± 1.73i	1.785 Hz	0.0194	3.52 s	19.94 s	-	-

All sections have negative real parts with spiral and dutch roll time being well within a large enough timeframe for the pilot to adjust according to the situation. As for the roll angle, Nelson [22] was once again used for the computation. Complying with AC 25-7D of the FAA, the roll time is 10.35 seconds at about δ_a of 5 degrees, which is below the 11 second requirement. The lateral OEI conditions are summarized in Table 42 and the roll time calculations are in Table 43.

Table 42 Lateral-Directional Control in OEI Conditions

Condition	δ_r trim
Takeoff	12.03 degs
Landing	4.10 degs

Table 43 Roll Time

Variable	Measurement
δ_r	5 degs
Roll Time	10.35 s

IX. Structures and Loads

A. Material Selection

The design of the major structural components of the team's aircraft was done with a factor of safety of 1.5 and a minimum margin of safety of 1, using the yield strength of the materials. The factor of safety complies with CFR §25.303 and is standard for military cargo aircraft along [25]. Aluminum alloys were used for their reliability, maintainability, and dependable life cycle. Composites were considered for this design, as is common for novel BWB propositions. However, the practical application and strict timeline laid out by the RFP demand a maintainable and easily produced airframe. The lifespan of aluminum and other metal alloys is far more predictable and easier to repair. Additionally, given the nature of military cargo loading, it is expected that peak pressures on the bay floor will exceed those predicted during nominal structural sizing. Introducing deformations in a metal cargo floor is far more desirable than introducing invisible cracks in a composite matrix. Instead, a titanium alloy was used for increased structural efficiency and weight savings throughout the aircraft, capturing a similar benefit to composites without the assessed risk. Thus, the additional safety and easier prediction of maintenance through the use of metals will allow Gravibus to stand out from other aircraft within the class.

The overall structural configuration of Gravibus uses standard aerospace aluminum and titanium alloys. The material selection for the major structural components and their mechanical properties are summarized in Table 44 with data from[26].

Table 44 Material Selection

Material	**Ultimate Yield Strength [Psi]**	**Ultimate Tensile Strength [Psi]**	**Density [lb/in^3]**	**Young's Modulus [ksi]**	**Component**
Al-2075-T6	73,000	83,000	0.102	10,400	Ribs and spars
Al-2014-T6	60,000	70,000	0.101	10,600	Skin, Pressure membrane
Ti-6Al-6V-2Sn (Annealed)	142,000	152,000	0.164	16,000	Longerons

B. Fuselage

The fuselage of Gravibus consists of a monocoque structure, with the skin bearing the majority of the structural load. This design choice provides weight savings and flexibility [27]. Two trusses resting above the pressure membrane connect the two outer wings together. The frame is spaced 500 inches apart, determined by the minimum distance that the pressure membrane could withstand, with a minimum thickness determined to be 0.097 inches for maximum weight savings. The cockpit is pressurized and has a frame spacing of 11.5 inches and a depth of 16 inches, as determined by [28]. The fuselage structure can be seen in Fig. 35.

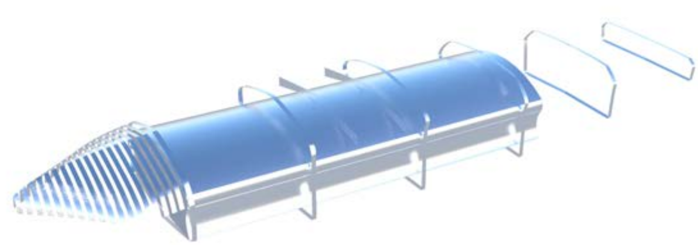

Fig. 35 Fuselage Structural Configuration

C. Pressure Membrane

The pressure membrane was designed for pressurization from FL080 to FL300 with a pressure difference calculated at 6.55 psi. The top of the membrane consists of an outer dome with a thickness of 0.097 inches tied with side walls 0.047 inches thick arced inwards to mitigate stress. There are two longerons running across the entire length of the membrane, tied between the intesection of the dome and the side walls. These titanium longerons provide structural integrity and weight savings for the thickness differences between the dome and sides. The bulkheads are placed forward and aft of the pressure membrane at the nose and empennage, respectively. There is also a bulkhead 15 feet from the forward location of the pressure membrane separating the cargo and PAX. The pressure membrane can be seen in Fig. 36. This pressure vessel design complies with CFR §25.841, providing cabin pressure at altitudes above 8,000 ft.

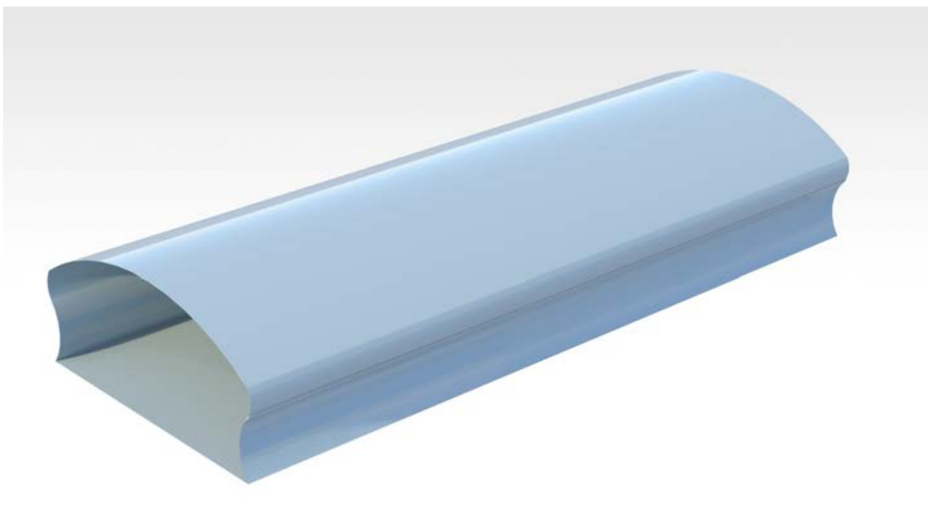

Fig. 36 Pressure Membrane

1. Side Wall Arc Trade Study

The design of the sides of the pressure membrane was investigated to provide optimal structural efficiency and weight savings. This was done by iterating on the number of arcs placed on the side, while maintaining a uniform thickness of 0.097 inches and distance of 500 inches. These geometric constraints were deemed optimal for weight savings and structural efficiency. Figure 37 shows a comparison between the Von-Mises stress of a flat side walls against one and two arcs respectively. Ultimately, one side arc was chosen as the final geometry for the pressure membrane due to its stress mitigation and overall weight compliance.

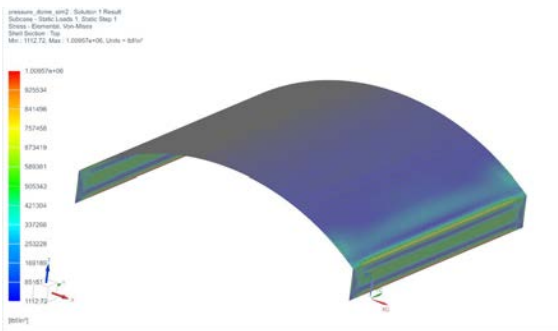

(a) Pressure Membrane with flat wall sides

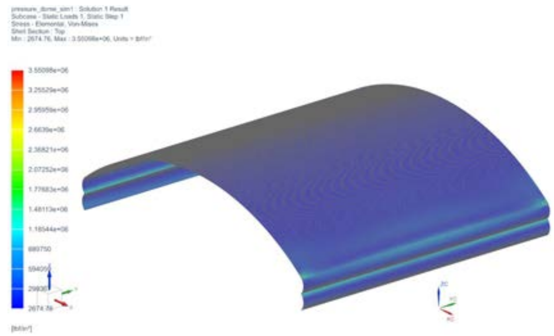

(b) Pressure Membrane with 2 Side Arcs

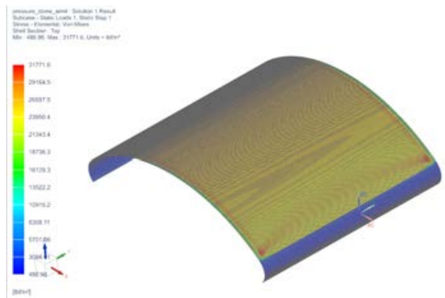

(c) Pressure Membrane with 1 Side Arc

Fig. 37 Comparison of Pressure Membrane Designs

D. Pressure Membrane Floor

To maximize weight savings and provide adequate space for the storage of the landing gear, the pressure membrane was designed to be supported by the cargo floor. The cargo floor consists of AL-2014-T6 squares, 33.75” x 35.47”, with a uniform thickness of 1/4 inch determined as the optimal geometry for structural efficiency and weight savings. Running between each square along the entire length and width of the cargo floor are titanium longerons tying the squares together. Figure 38 depicts the FEA results of the floor.

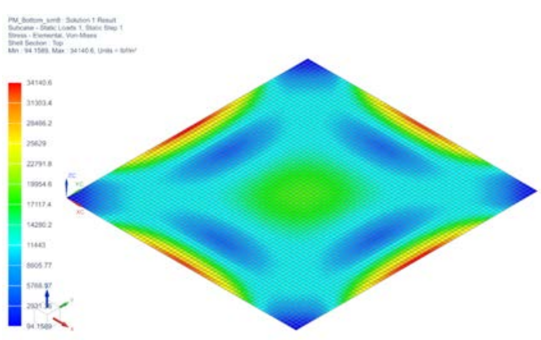

Fig. 38 Al-2014-T6 Square 33.75” x 35.47”

E. Wing-box

The wing-box consists of a front and rear spar located 15 and 70 percent of the chord respectively based on [28]. The ribs are equally spaced 30 inches apart based on similarity analysis from the C-5 [28]. Ribs are placed streamwise to the spars between the root and tip and cut outs outside of the spars were made for the leading edge slats, flaps and ailerons. Rib thicknesses were determined by analyzing the shear flow in each panel and the thickness was tapered linearly from the root to the tip. The root rib thickness was determined to 0.273 inches and the tip rib thickness was determined to be 0.150 inches. Table 45 is a summary of the spar geometries.

Table 45 Spar Geometry Parameters

Component	Width [inches]	Height [inches]	Cross-section area [in^2]
Root Front Spar Cap	3	0.50	1.50
Root Rear Spar Cap	3	0.50	1.50
Tip Front Spar Cap	2	0.50	1.0
Tip Rear Spar Cap	2	0.50	1.0
Root Front Spar web	0.50	36.0	18.0
Root Rear Spar web	0.50	30.0	15.0
Tip Front Spar web	0.50	10.65	5.325
Tip Rear Spar web	0.50	8.0	4.0

An elliptical lift distribution with a design limit load of 4.5 was simulated for the front and rear spar geometry. The front spar was determined to take 77 percent of the lift while the rear spar 23 percent. Figure 39 depicts the wing structural configuration, and Fig. 40 depicts the results of FEA analysis of the wing structure.

Fig. 39 Outer-Wing Structural Configuration

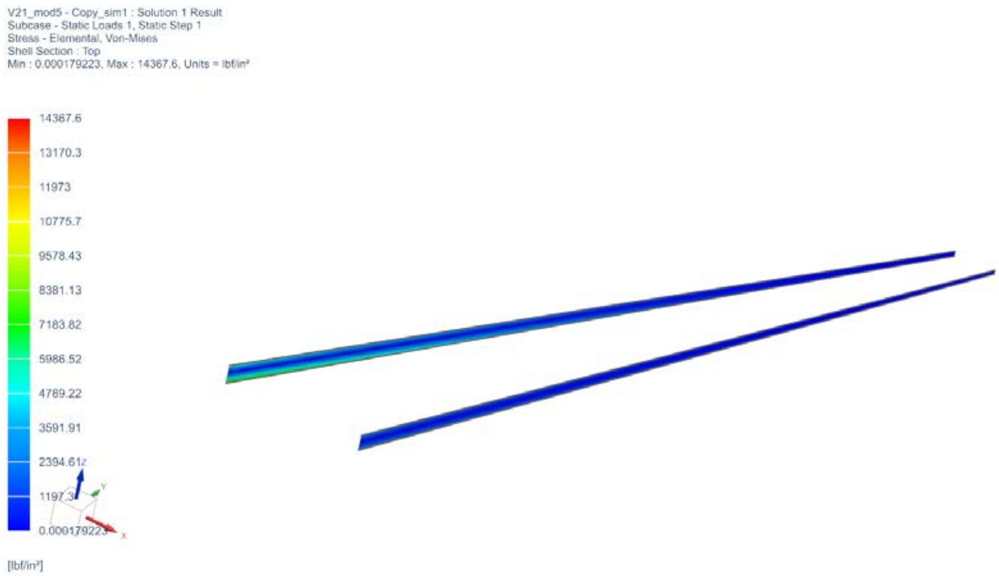

Fig. 40 Outer Wing FEA Resultss

Fig. 41 Outer Wing Structure and FEA Analysis of Outer Wing

F. Horizontal and Vertical Tail

The horizontal and vertical tail front spar were sized empirically similar to the outer wing design based on [28]. The rear spar was optimized to fit the control surfaces. The ribs are spaced 24 inches apart based on [28]. Figure 42 depicts the structure of both the horizontal and vertical tails.

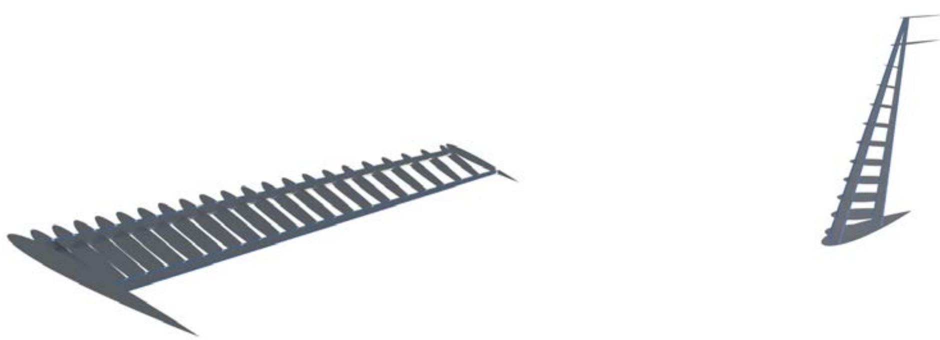

(a) Horizontal Tail **(b) Vertical Tail**

Fig. 42 Empennage Structure

G. Truss Structure

When designing the Gravibus one of the most significant challenges was the structure of the inner wing / fuselage. BWB propositions available for the team to study all tackled the pressurized inner wing in the same way. The typical approach is to lay the fuselage out with ribs dividing it into sections like a traditional wing. With the cargo capabilites requiring a greater enclosed volume of a BWB configuration the team opted to divorce the inner wing torque structure and the pressure membrane. With the pressure membrane self sufficient, the torque structure could take a free form geometry. It was determined that an extremely efficient and easy to produce structure would be a triangular truss connecting the load bearing points of the fuselage together. A truss was located on each side of the pressure vessel, running lengthwise down the fuselage.

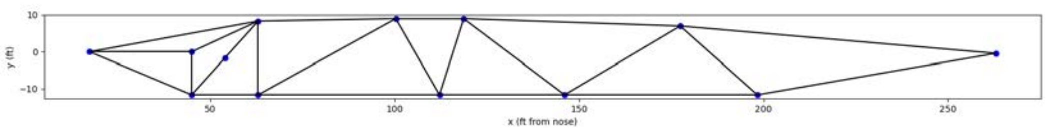

Fig. 43 Truss Structure Shape

The truss was sized using static analysis. Once Gravibus had taken shape, the points were analyzed to form a series static constraints. For Gravibus, the total of 23 members constrained by 13 points in two axes creates an over constrained linear system of the form:

$$\Sigma F_{ext} = CF_{members}$$

where, for i nodes and j members

$$F_{ext} = \begin{bmatrix} F_{ext,z,0} \\ \vdots \\ F_{ext,z,i} \\ F_{ext,x,0} \\ \vdots \\ F_{ext,x,i} \end{bmatrix} \text{ and, } F_{members} = \begin{bmatrix} F_{member,0} \\ \vdots \\ F_{member,j} \end{bmatrix}$$

Generating a coefficient matrix C for our design and using the pseudo-inverse to solve for the lowest norm solution to the loading case, the forces present in each member were computed. By solving for the flying (N_{ULT} = 4.5) and parked loading conditions and taking the greater compressive and tensile force for each member, a minimum area could be calculated based on the yield strength of the chosen design material: Ti-6Al-6V-2Sn. Multiplying this area by the length of each member and the density of the chosen Titanium alloy - a final weight was calculated for the truss system of 38,000 lbs. Titanium was chosen due to the weight savings offered, but mostly due to the volumetric limitations in the small transition space of the plane from the fuselage to wing cross sections.

H. Overall structural configuration

The overall structural configuration of Gravibus with the fuselage, wing-box, truss structure, propulsion system, horizontal and vertical tails and pressure membrane is shown in Fig. 44.

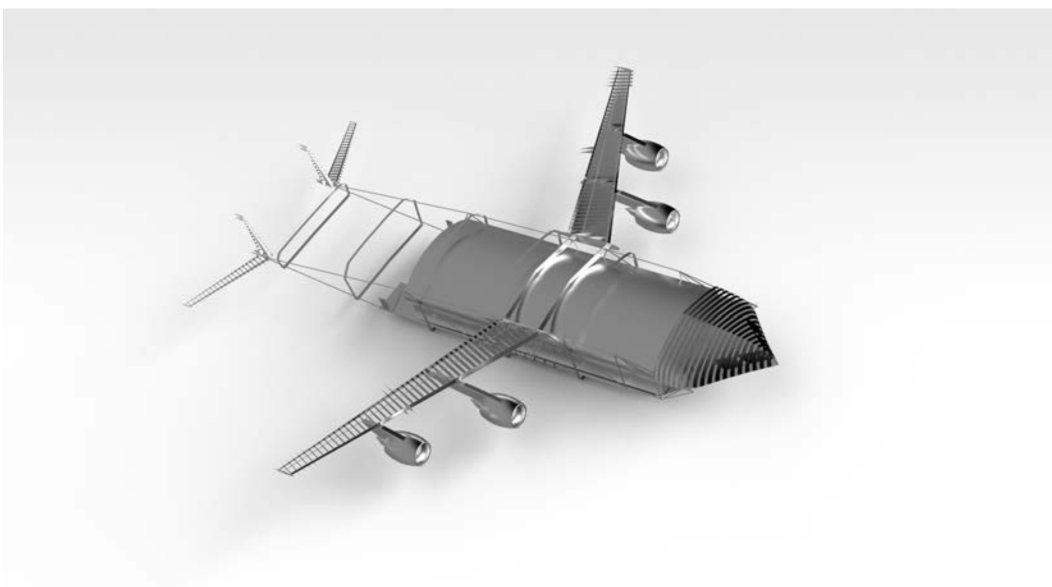

Fig. 44 Gravibus Overall Structural Configuration

I. V-n Diagram

Figure 45 shows the V-n Diagram which provides a visual representation of the aircraft's structural capabilities and limitations depending on the aircraft's maneuvering speed (V) and the aircraft's load factor (n) for the aircraft. The diagram is plotted with the equivalent airspeed (in knots) on the x-axis and the load factor (n) on the y-axis. A limit load factor of 3 and -1.5 and an ultimate load factor of 4.5 and -2.25 with a safety factor of 1.5 were used per the RFP.

The safe envelope, the area inside the lines, defines the region within which the aircraft can operate safely without experiencing structural damage or stall. The structural damage region and the aircraft failure regions are outlined as well. The left corner points of the safe envelope each represent the stall region at positive and negative load factors while the right corner points represent the structural failure area at positive and negative factors. The dashed lines represent the gust load lines at Vb, Vc, and Vd on the aircraft's load factor. Key values used for designing the V-n diagram are listed in Table 46.

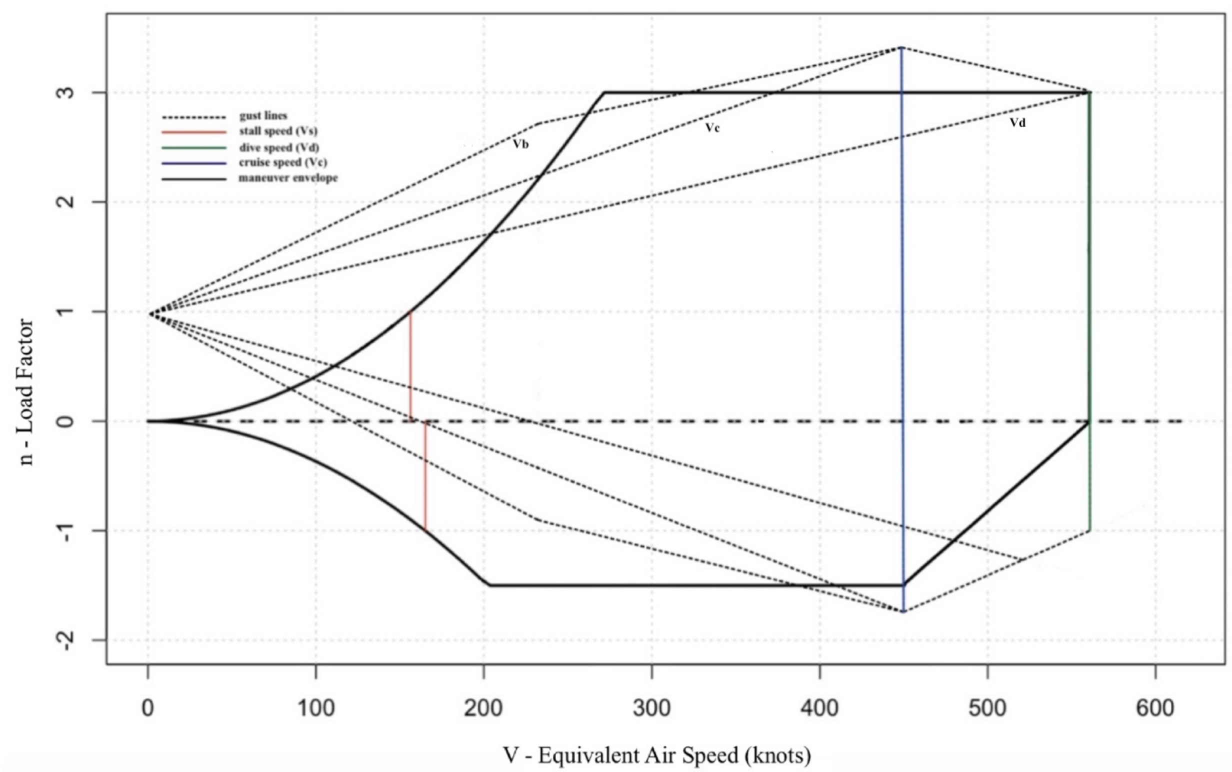

Fig. 45 V-n Diagram

Table 46 Key Values from V-n Diagram

Parameter	Value
$V_{S+}(KEAS)$	156
$V_{S-}(KEAS)$	165
$V_C(KEAS)$	448
$V_D(KEAS)$	560
μ_g	88
k_g	0.8
$g(ft/s^2)$	32.2

The cruise altitude is 35,000 ft. The stall speed (Vs) was calculated by setting the weight equal to the lift at a load factor of 1. Dive speed, which was designed to be 25% higher than that of the design cruise speed according to Roskam[28], indicates the maximum air speed at which the aircraft can be operated without exceeding its structural limits due to the loading from dynamic pressure. This value was used as it is the common dive speed calculation for transport aircraft. The structural failure zone represents the region that would exceed the aircraft's structural limits, leading to catastrophic failure or structural damage, while the structural damage zone indicates the speed at which the aircraft may not have immediate catastrophic failure but could result in cumulative structural damage over time.

This diagram was conducted using the MTOW of the aircraft. The aircraft's weight at the cruise level would be less than the MTOW due to the burn of fuel, and the actual loads experienced will be lower than those represented in the V-n diagram based on MTOW. Using the MTOW for V-n diagram is justified for conservative design purposes and to ensure structural integrity under the most critical loading conditions, presenting the worst-case scenario. By designing and certifying the team's aircraft to operate within the safe envelope at MTOW, it ensures that the structure can withstand the highest anticipated loads throughout the flight, including during takeoff, landing, and maneuvering, when the aircraft is at its heaviest weight.

J. Load Path Analysis

Figure 46 illustrates the load paths for both cruise and ground operations of Gravibus.

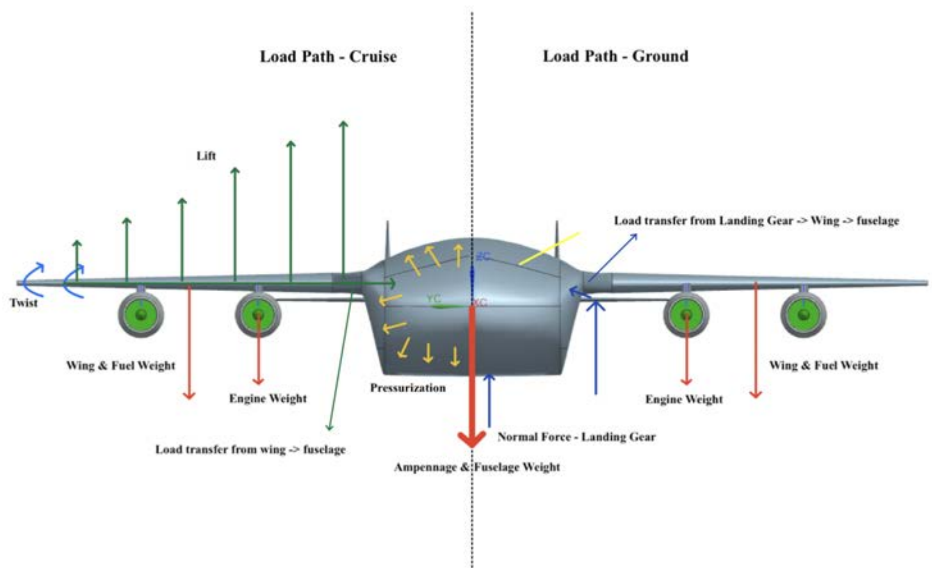

Fig. 46 Load Path at Cruise and Ground

At cruise, the primary load path begins with the lift force generated by the wing. The lift force on the wings and the downward forces applied on the engines and fuels in the wing box will be transferred through the front and rear spars of the aircraft's wing box structure. The loads are then transferred from the wing to the fuselage through structural reinforcements at the wing-fuselage junction. The weight of the payload will be applied directly to the fuselage structure. It will be distributed along the CG by the longitudinal fuselage longerons, which will transfer the loads to the frames and pressure membrane.

Additionally, the weight of the wing and fuel affects the load distribution, creating bending and torsional moments. These loads are transferred through the internal structure of the wing and fuselage, ultimately reaching the Gravibus's center of gravity. The thrust generated by the engines also plays a role in the load path during cruise. The engine weight and thrust loads are transferred through the engine mounts and reinforced structures within the fuselage and wing-fuselage junction. These loads will then pass through the middle wing box, and be distributed along the fuselage longerons, frames, and pressure membrane to the center of gravity.

During ground operations, such as landing or taxiing, the load path differs significantly from the cruise condition. The primary load transfer will occur from the landing gear to the wing and fuselage structures.The normal force acting on the landing gear will be transferred through the landing gear struts and attachments to the wing and fuselage structures. The weight of the aircraft, including the wing, fuel, engines, and other components, also contributes to the load distribution during ground operations. These loads will be then transferred through the wing and fuselage structures, eventually reaching the landing gear.

K. Load Cases

1. Wing

The wing bending moment graph was generated by XFLR and is shown in Fig 47. The bending moment caused by the lift distribution will be primarily carried by the front and rear spars, which will transfer these loads to the wing-fuselage junction. From there, the bending moments will be distributed along the fuselage longerons, frames, and pressure membrane towards the CG.

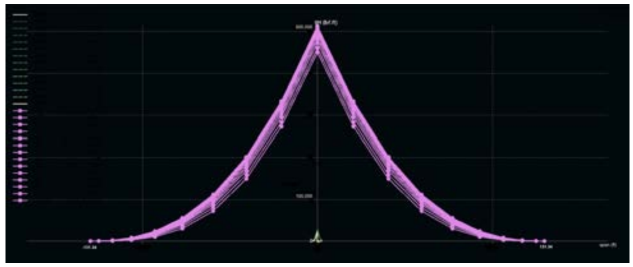

Fig. 47 Wing Bending Moment

2. *Truss*

Figure 48 depicts the fuselage truss design for Gravibus. The forces acting on each member are indicated, along with their respective diameters, weights, and whether they are experiencing compression or tension.

Fig. 48 Fuselage Truss Design

Starting from the nose of the aircraft (node 0), the truss diagram shows a compression force of 1,041,742 lbs acting on a member with a diameter of 3 inches and a weight of 373 lbs. This force is due to the aerodynamic loads on the forward fuselage section and the weight of the aircraft components in that region. Moving towards the wing-fuselage junction, member 9 and member 13 will be experiencing compression loads, which would be attributed to the bending moments and lift forces acting on the wing structure. The wing-fuselage junction is a critical area where the loads from the wings are transferred to the fuselage. Members such as 10 and 12 will experience significant compression loads as they transfer the wing loads into the fuselage, requiring robust structural reinforcement in this area. The nose and aft sections of the fuselage also experience substantial compression and tension loads due to aerodynamic forces, landing gear loads, and tail surface loads. Throughout this simplified truss diagram, critical load paths and load distribution patterns throughout the fuselage structure can be observed.

3. Landing Gear

The landing forces applied to the aircraft during its taxiing, touchdown, and takeoff will be initially received by the aft landing gears. These loads will then be transferred through the landing gear support structures and distributed along the wing, fuselage frames, longerons, and pressure membrane towards the CG. The landing gears are therefore designed to withstand the high vertical force during the landing and transfer the load to the fuselage structure without causing damage to the structure, as further mentioned in the team's Landing Gear section. The locations of the landing gear are shown in Fig. 49. Table 47 present the dimensional specifications, load limits, and maximum load applied during operation for the nose and main landing gear tires.

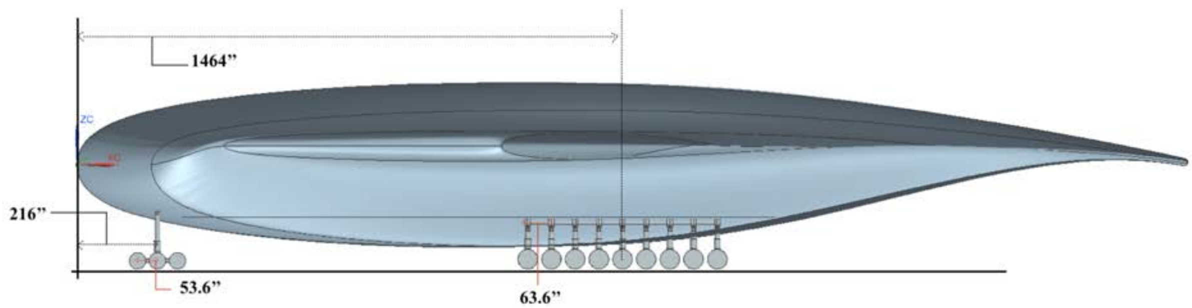

Fig. 49 Landing Gear Location

Table 47 Tire Load Limits and Applied Loads

	Nose Tire	Main Tire
Diameter [in]	44.3	53
Width [in]	15.05	20.1
Area [sq. in]	187.07	322.80
Inflation [psi]	210	212
Load Limit [lb]	39,285	68,433
Load Applied [lb]	38,780	65,854

The trunnions, where are the primary connection points where the landing gear struts attach to the fuselage, will be produced using titanium to be robust enough to transfer the high landing loads from the struts into the airframe. Additionally, to effectively transfer the side loads and torque moments generated during operation, torque arms will be also designed with titanium alloys to withstand the substantial loads without yielding or fracturing. They will be firmly attached to the landing gear strut assembly with a pinned joint.

4. Pressurization

The pressurization forces acting on the interior walls of the pressure membrane will be distributed throughout the arcs of the pressure membrane structure and the fuselage frames that provide additional support for the part. With an area of 2,592 square inches and a pressure differential of 6.55 psi, the cabin pressurization load acting on the cabin door will be 16,978 lbs. This concentrated load from the cabin door shall be transferred through the local reinforcing structures around the door opening, including reinforced frames and longerons, ultimately transferring the load to the aircraft's CG. Similarly, the cargo door will experience an even larger pressurization load due to its larger area. With a surface area of 372,250 square inches and the same 6.55 psi pressure differential, the total force acting on the cargo door will be 2,438,238 lbs. To manage this significant pressurization loads on the cargo door, thicker frames and reinforced longerons will be used around the cargo door opening to transfer the concentrated loads into the surrounding fuselage structure. There will be additional floor beams beneath the cargo floor to transfer the loads from the door into the fuselage frames and longerons.

X. Mass Properties

After deciding to go forward with a non-traditional configuration, the team was not able to rely on well proven empirical methods instead relying on a purely theoretical mass estimation[7]. This estimation uses first principle techniques and some assumptions to idealize the structure of a BWB aircraft. Ultimately, it was determined that the team's configuration did not blend the body and wing in the same way outlined by Howe. Because the outer wing had taken the shape of a traditional trapezoidal wing and the body had little sweep, the team found that combining Howe's estimations with Roskam Class II methods yielded results closer to the weights generated during initial designs of the wing box and pressure structures. The Howe model proved sensitive to certain wing parameters, while the Roskam equations kept reasonable results throughout the aircraft's potential domain.The final sizing loop used Roskam for the wing and any BWB independent systems, and the Howe model was used for fuselage and pressure member estimation.

However, in this later stage of the design, a majority of component weights are confidently calculated using high fidelity CAD measurements. The weight of systems for which an accurate 3D model has not been produced were calculated using the empirical Class II weight methods outlined in Roskam, [28] and the theoretical weight methods outlined in Howe's "Blended wing body airframe mass prediction" [7]. The empirical nature of the Roskam Class II methods gives confidence to their results, while the theoretical nature of the Howe paper lends uncertainty to values taken from it. However, once past the uncertainty of initial design, the designed structure passed load analysis allowing the team to use accurate weight methods by assigning materials to fully modeled, digital components. All components were represented in 3 dimensions to allow for accurate calculation of the aircraft center of gravity from a part by part breakdown. The results of the significant measurements are outlined in Table 48. It should be noted that the nose system's weight is a sum of the Roskam instrumentation weights and the actual reported weights of the selected Avionics package.

Table 48 Component Weight Breakdown

Component	Weight (lbs)	Weight Measurement	CG Description	X_{cg} (ft from nose)
Pressure Vessel	57,000	CAD Measurement	Pressurized Centroid	112
Bulkheads	39,550	Howe Eq.41	Pressurized Centroid	112
Cargo Floor	39,550	CAD Measurement	Cargo Centroid	119
Fuselage Truss	38,080	Static Analysis	Pressurized Centroid	134
Fuselage Truss	39,550	Static Analysis	Pressurized Centroid	112
Wing Structure	50,480	CAD Measurement	CAD Centroid	132
Engines	96,640	Reported Weight	CAD Centroid	132
Skin	33,680	CAD Measurement	CAD Centroid	135
Horizontal Tail	2,770	CAD Measurement	CAD Centroid	257
Vertical Tail	2,730	CAD Measurement	CAD Centroid	257
Nose Gear	6,650	Roskam Class II	CAD Centroid	9
Main Gear	37,700	Roskam Class II	CAD Centroid	122
Nose Systems	3,540	Reported+Roskam Class II	CAD Centroid	14
Belly Systems	29,850	Roskam Class II	CAD Centroid	125
Skin Support	27,600	Howe Eq.22	CAD Centroid	126
Total Empty	**475,000**	Summation	Weighted Average	**118**
Max Payload	430,000	Requirement	Cargo Centroid	119
2,500nm Fuel load	212,000	Sizing Algorithm	Outer Wingbox Centroid	129
5,000nm Fuel load	389,300	Sizing Algorithm	Outer Wingbox Centroid	129
8,000nm Fuel load	229,000	Sizing Algorithm	Outer Wingbox Centroid	129
MTOW	**1,160,000**	$W_e + 295,000 + \text{fuel}$	Weighted Average	**124**

The CG variance of the aircraft during the design required missions is shown in Fig. 50. Due the 25 °sweep of the wing quarter-chord, and the large fuel requirements associated with such a large aircraft, the in-flight CG variation is somewhat large. This large, and unavoidable, variation in CG due to fuel burn must be considered during the loading of the aircraft.

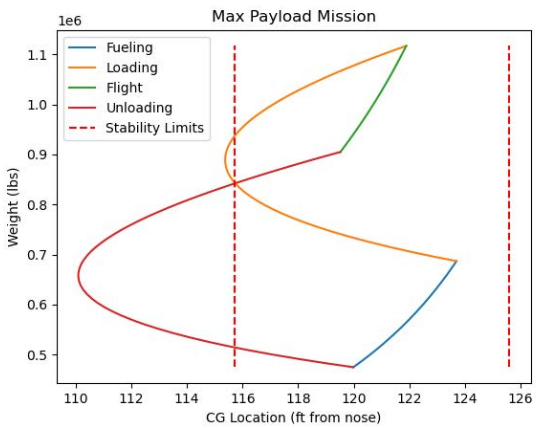

(a) Max Payload Mission

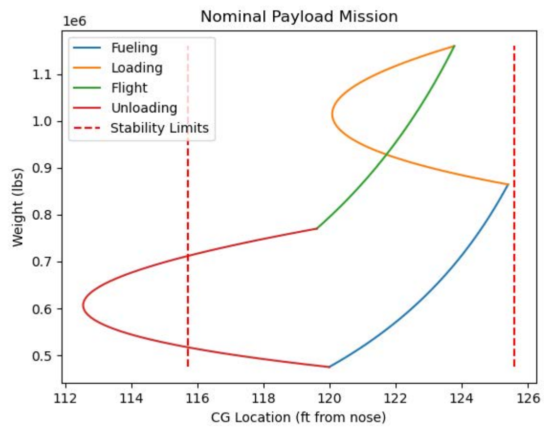

(b) Nominal Payload Mission

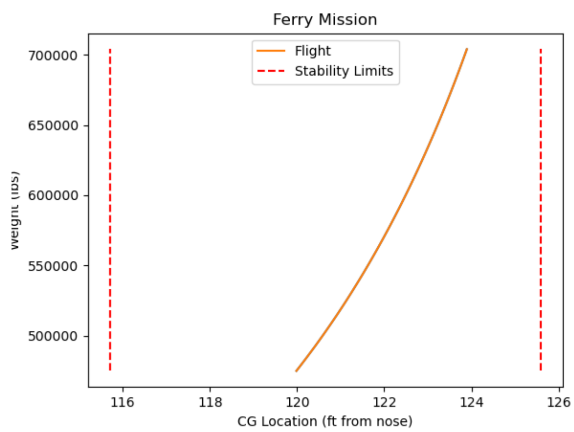

(c) Ferry Mission

Fig. 50 CG Variation for RFP Mandated Missions

These missions are represented with a payload of the mandated weight, distributed evenly throughout the aircraft's pallet configuration. The CG is calculated for the condition of each row of pallets being loaded to the front of the available space, and removed by the rear most row at a time. As such, it can be observed that placing cargo at the front of the cargo bay without consideration of the fuel load and cargo CG location could lead to an unstable flight condition.

XI. Landing Gear

A. Configuration

Gravibus' landing gear are in the tricycle configuration following similarity to other heavy lift aircraft like the AN-225 or C5-Galaxy. Landing gear loads were calculated according to Raymer Chapter 11 [3]. Once the loads for the main and nose gear were determined, a trade study of hundreds of different tire sizes [29] was conducted to determine the lightest configuration. The analysis first determined the load that each tire could support. Then the minimum even amount of that tire was necessary to support the total load was determined. Lastly, the weight of all the tires necessary to support its weight was calculated and used to determine which choice of tires was the lightest. Table 49 summarizes the tires chosen for the nose and main gear. In total, the weight of all the tires in the landing gear weights 11,500 lbs. Both types of tires are below the 220 psi inflation limit set in the RFP [1]

Table 49 Selected Tire Sizes

Tire Parameter	Main Gear	Nose Gear
Size	H25x21.0-24	46x16
Diameter [in]	53	44.3
Width [in]	20.1	15.05
Contact Area [in^2]	322.8	187.1
Inflation Pressure [psi]	212	210
Load [lbf]	68,433	39,285
Tire Weight [lb]	293.7	154.4
Number of Tires	36	6

B. Retraction

Figure 51 illustrates the landing gear in the extended and retracted position. The main gears fold in towards the center of the fuselage. The nose gear rotate forward and up towards the nose of the plane, resting beneath the cockpit.

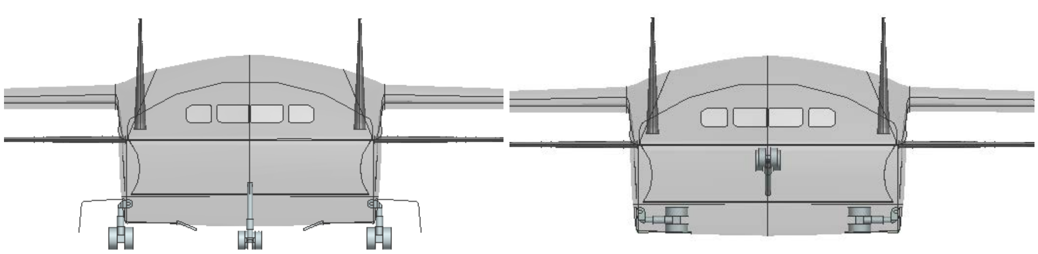

Fig. 51 Landing Gear Retraction Scheme

C. Ground Clearances

Figures 52, 53, and 54 depict the tailstrike, ground roll, and overturn angles. The tipback angle of 15.663 °is greater than the tailstrike angle, as well as 15 °as specified in Raymer [3]. The overturn angle of 42.866 °as seen in figure 54 is less than the 63 °limit as specified in Raymer [3].

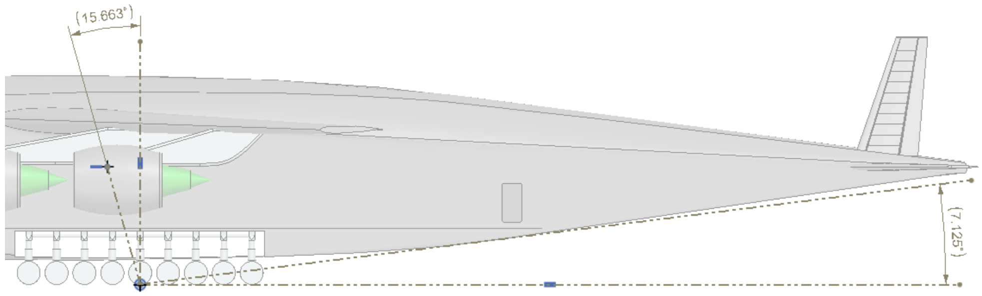

Fig. 52 Tailstrike and Tipback Angles

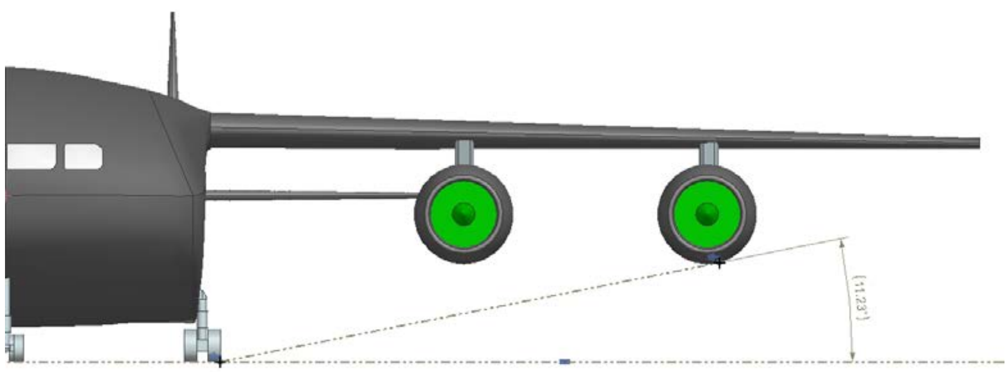

Fig. 53 Ground Roll Clearance

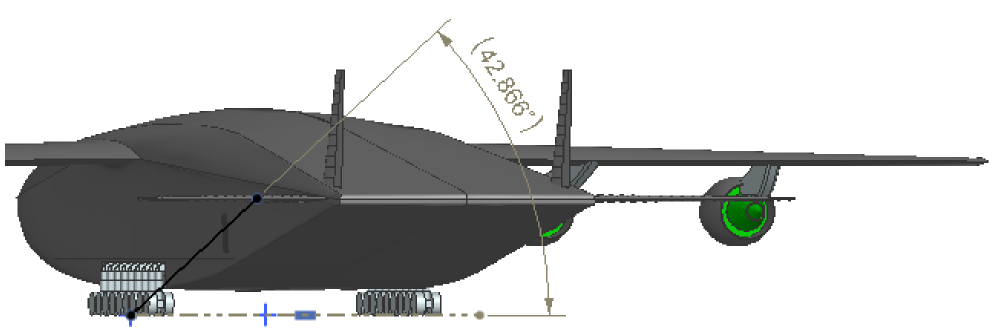

Fig. 54 Overturn Angle

D. Turn Radii

Figure 55 illustrates the turning radii in inches of the Gravibus during taxi. Gravibus requires a width of at least 180 ft in order to make a 180°turn, meaning a turning platform would be needed to assist Gravibus for 180°maneuvers. Gravibus features steerable nose and main gear that can rotate at each independent bogey to enable tight turns. In order to rotate 180°within the 180 ft width, the nose gear must be rotated 70°and the greatest rotation from a main gear bogey is 44°. During this maneuver the tail tip will travel across an arc that is 380 ft in diameter.

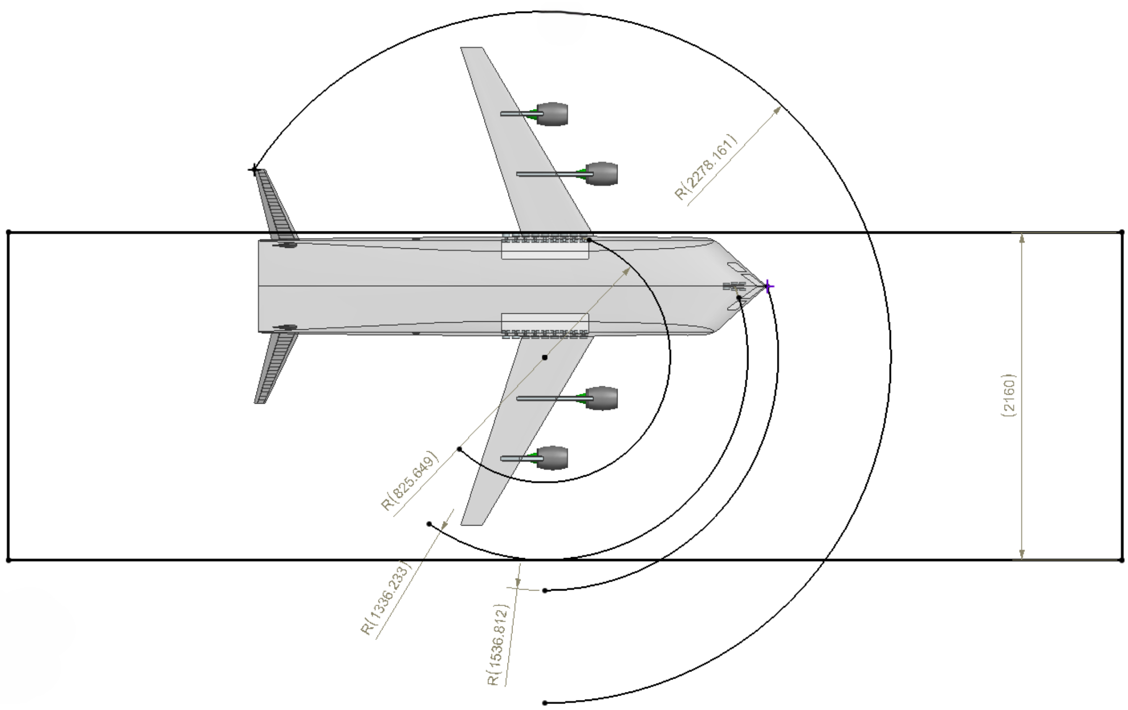

Fig. 55 Turning Radii

XII. Systems

A. Hydraulics Layout

The control surfaces of Gravibus are hydraulically actuated, depending on one of three independent hydraulic loops. Each engine pair (per wing) will be responsible for one mechanically pumped loop, while the bottom of the aircraft contains an electric pump and corresponding hydraulic loop. All loops will be capable of supplying pressure to all control surfaces, through a unique actuator. Figures 56 and 57 depict the hydraulic layout.

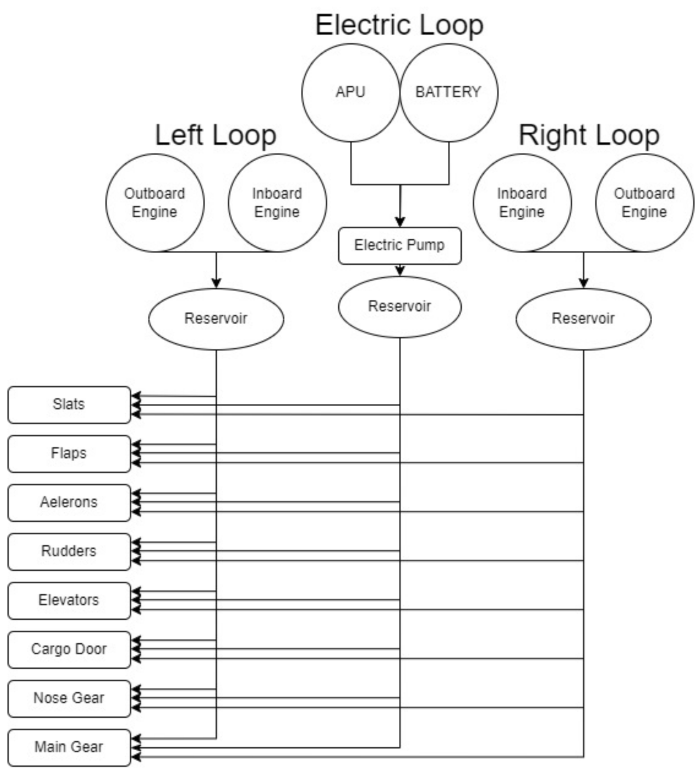

Fig. 56 Hydraulic System Overview

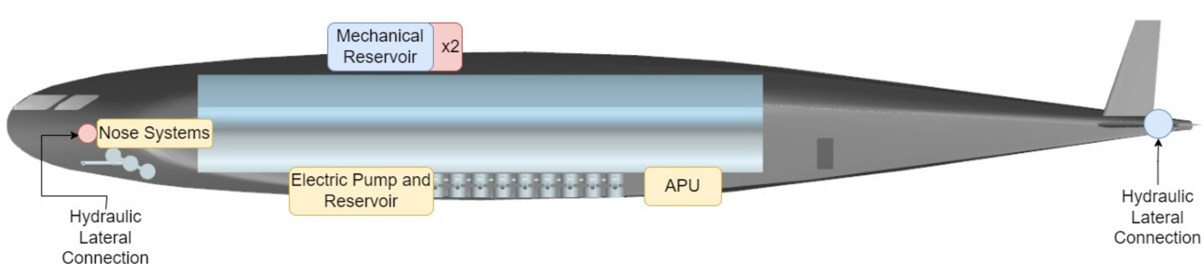

Fig. 57 Hydraulic System Side View

Each hydraulic loop occupies as much of it's own unique space as possible, to minimize the likelihood of a single catastrophic event from disabling the entire aircraft's control authority. To accomplish this, the electric loop runs along the bottom-center of the aircraft branching out as needed. Conversely, the two mechanical loops occupy the left and right sides of the fuselage above the cargo bay, with the right hand loop connecting to the left wing by routing around the front of the aircraft and the left hand loop connecting to the right wing by routing around the back of the aircraft. This is done so that an impact to the center of the aircraft cannot sever both hydraulic loops as the lateral connections are separated by 200 ft of airframe. All loops operate at 3,000 psi with a flow rate of 100 gpm. Engine power requirements were taken as the power required to achieve this flow rate and pressure, at an engine pump efficiency of 85%, giving an estimated mechanical draw of 204 HP per wing. This flow rate and pressure was found through similarity, having the same pressure and an increased flow rate with respect to the Boeing 747-100.

B. Electronics Layout

Gravibus employs 3 completely independent electrical power sources: the right wing, left wing, and the APU. All power sources feed to a main bus where their outputs are converted to DC for use in the aircraft battery systems. All power sources are to have their own wiring independently fed to this central system. Wherein the nose, two isolated electrical systems will draw from the main DC current to charge their own batteries and maintain their own flight computer. Also available to power these systems is a ground power connection located under the nose, near the forward gear of the aircraft. The electronic system layout is depicted in Fig. 58.

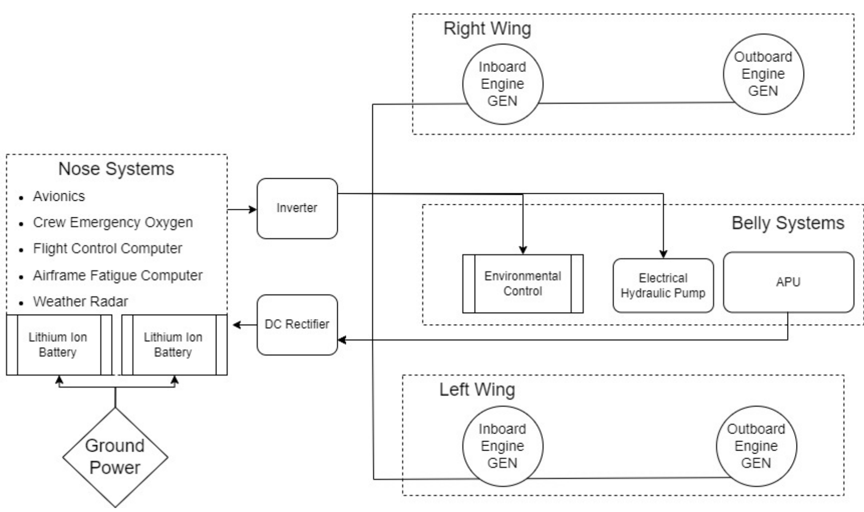

Fig. 58 Electronic System Overview

The electronics system is designed to be able to provide the necessary power to the electronic hydraulic loop with only two engine's electrical power available. This ensures that only one wing must maintain electrical connection to power the flight required systems, additionally this allows generators to be run significantly under max load during normal flight, extending their operating lives. This drove the maximum instantaneous load of the engines generators to be in excess of the 204 HP required for our hydraulic pump rate. The load of additional systems has not been qualitatively computed, however leaving an excess of roughly 100 HP per loop on top of the hydraulic power requirement safely ensures the ability of the aircraft to operate continuously under generator power. This output is well within the auxiliary gear pad maximum continuous output specified in Section V.

C. Pneumatic System

Gravibus will employ bleed air pneumatics from each of the four available engines. The outboard engine bleed air will be preconditioned by being routed through the leading edge slats in order to cool the air before the central heat-exchanger and environmental control. The inboard engine air will be routed through the flaps before entering the fuselage. This preconditioning lowers the required work of the environmental control heat-exchangers while also providing de-icing capabilities to the aircraft. Additional bleed air routes will be available for the ailerons, to bypass the control surface de-icing routes, and a computer driven relief solenoid. The nature of passing fluid through a moving joint, as is done for our leading edge slat de-icing, ensures that some bleed air will be lost to atmosphere. This is the reason the system will include a direct bypass to the fuselage, however, it is expected that similar to fuselage pressure losses, these small losses in the hinges will have little effect on the overall system. Ram air ducting is employed along the bottom edges of the aircraft to facilitate heat exchange to fully condition the engine bleed air for use by the environmental control systems. Each fresh air duct is also routed centrally to the intake of the APU to allow its use in flight. The pneumatic and ECS systems are shown in Fig. 59.

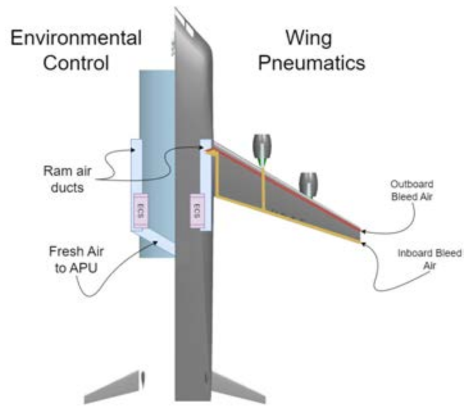

Fig. 59 Pneumatic and Environmental Control System

D. Fuel System and Wing Integration

The wing tanks have a measured fuel capacity of nearly 525,000 lbs. Some of this extra capacity will be utilized for self-sealing fuel tank linings, while the remainder serves as ample room to add additional actuators or hydraulic systems in the wing if additional redundancy was desired at any point during production. To facilitate fuel flow in the wing box. the ribbing has holes at the bottom of each rib. However, if any issues with fuel delivery arise during production, this extra volume could be used to implement a greater network of transfer pumps. The fuel system and its integration in the wing are depicted in Fig. 60.

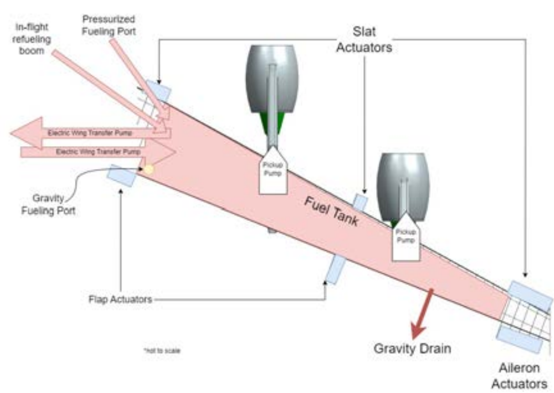

Fig. 60 Wing Systems Diagram

During flight the fuel will be balanced between both wings by transfer pumps, which are also responsible for distributing the incoming fuel during pressurized ground refuelling. Gravity fueling can be performed through a direct access point into each wing, rather than the lower fueling port on the side of the aircraft which requires a pressurized fuel supply.

XIII. Avionics

The avionic systems were chosen to meet the requirements established by RFP. These systems comply with the requirements of being consumer-off-the-shelf and certified to fit the needs of the aircraft. The selections for the avionics system are summarized in Table 50, which details the sizing, weight, power, and temperature limits for all of the avionics used in the system. The rationale behind the selection of system was mainly to implement trusted systems that have been previously used on other military aircraft while also having the size and weight be negligible when it comes to shifting the center of gravity.

Table 50 SCHWAP table

Component	Category	Model	Size [in]	Weight [lb]	Power [W]
GPS	Navigation	Honeywell H-764	7 x 7 x 9.8	20	30-60
INS	Navigation	Honeywell N580	3.54 x 2.36 x 2.36	1.10	7.5
TACAN	Navigation	L3Harris TACAN+	4.97 x 3.45 x 10.75	5.6	500
TFR	Management	Mark XXII EGPWS	3.25 x 0.8 x 3.20	0.5	48
Display	Comm.	Honeywell DU-875	8 x 7	7 (each)	
VHF	Comm.	Collins VOR-900	3.74 x 7.64 x 12.76	9.0	12
SATCOM	Comm.	Collins IRT-4000	15.26 x 2.43 x 7.87	7.7	125
IFF	Comm.	Collins APX-119	5.37 x 5.37 x 8.37	10	50
Warning system	Defense	BAE AN/AAR-57	9.1 x 5.5 10.7	19	111
Weather Radar	Defense	BAE AN/ALE-47		29.05	70

A. Flight Deck

The design of the flight deck is critical in ensuring that the aircraft can be operated safely, comfortably, and efficiently. Per the RFP requirements, the flight deck is set up to operate with a pilot and co-pilot, and crew quarters are provided for the two loadmasters as well as an entire relief crew [1]. The RFP states that Zero-Zero crew systems may be provided, but are not required [1]; Gravibus will not feature these systems due to the additional weight and systems required. The flight deck layout is designed for crew comfort as well as to meet all FAA requirements. The FAA CFR § 25.773 states that the compartment must be set up to give "pilots a sufficiently extensive, clear, and undistorted view, to enable them to safely perform any maneuvers" [25]. Due to the unique nose shape of the BWB design, some of the viewing angles must be provided digitally, as opposed to views available purely from the windows of the aircraft. Thus, cameras are installed to view angles not possible from the windows with corresponding displays in the flight deck. Further, the cockpit controls are laid out to comply with FAR §25.777. The flight deck layout can be seen in Fig. 61.

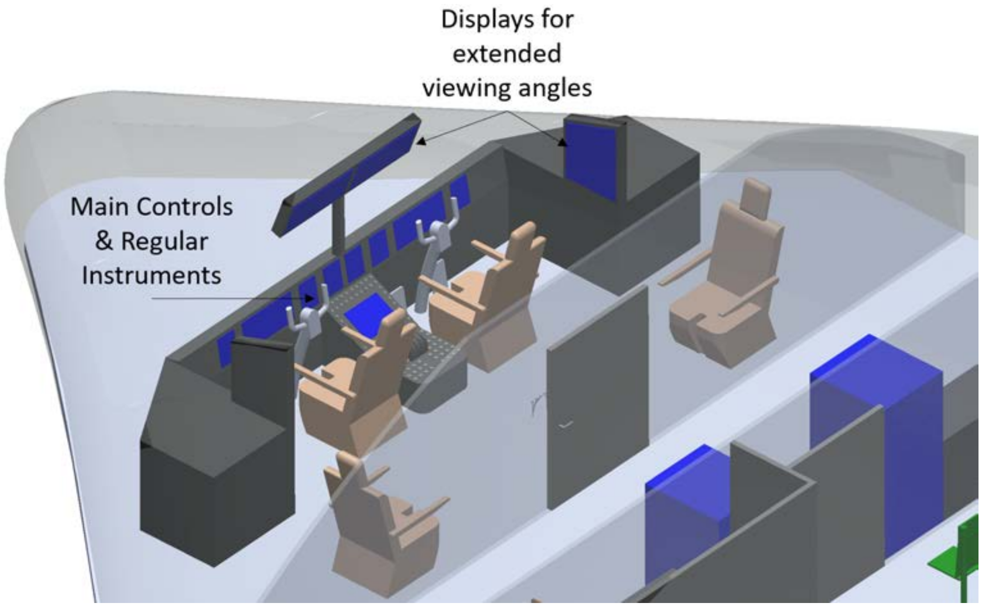

Fig. 61 Flight Deck Layout

XIV. Repair and Maintenance

The repair and maintenance of Gravibus will balance frequent preventive maintenance with the required Maintenance Man Hours per Flight Hour (MMH/FH) outlined in the RFP, which can be no greater than 24 MMH/FH [1]. The primary mechanism for preventative maintenance will be home station checks (HSC) and the use of the novel digital twin technology. Gravibus is intended to fly with onboard thermal and mechanical strain sensors located along the spars, fuselage truss, and cargo floor. Data from these sensors can be combined with flight control data to virtually recreate the fatigue of the aircraft on a per flight basis, accumulating into a "digital twin" of each GraviBus in service. This system would also allow maintenance crews to monitor for unusual fatigue or load situations. It is expected that data from this system will have a cumulative effect of refining the failure points and common fatigue locations over the lifetime of the aircraft [30]. However, lacking a high fidelity method to quantify the benefits and rate of data acquisition, the digital twin system, and associated sensors are not factored into quantitative analysis of MMH/FH.

Rather than rely on the novel digital twin system, it will instead be used to augment the traditional maintenance process of HSCs. These checks will occur at a similar frequency to the C-17, every 180 days [31]. These frequent HSCs, along with daily line checks, and the digital twin, should allow for preventative maintenance to occur consistently and allow Gravibus to remain operationally available an overwhelming percentage of the time. Further, the internal configuration of Gravibus will allow for easy access to inspections and repair of the plane. A majority of systems can be accessed directly beneath the plane; namely, the environmental control, APU, and nose systems are directly accessible once the aircraft has been placed on jacks. The Gravibus Has six primary jack points; four on the ends of the main gear assembly, and two at the nose of the aircraft just forward of the PAX pressure bulkhead. These locations were chosen as they are directly tied to the fuselage truss. Moreover, systems will take advantage of the use of line removable units (LRUs) when applicable. The avionics system was selected with this ease of maintenance in mind, all control surface actuators will be designed to be LRUs, and electrical components such as breakers and generators will be designed with efficient removal in mind.

Following typical aviation maintenance schedules, the maintenance will be split up into line, A, B, C, and D regular checks with additional consideration for more complex systems and unscheduled repairs. Estimates for the frequency and duration of these checks are based on averages from the aviation industry [32] scaled to the size of our aircraft. Table 51 details all the maintenance types and their respective MMH/FH.

Table 51 Maintenance Table

Type	**Frequency (Flight Hours)**	**Labor (Man Hours)**	**MMH/FH**
Line	6	6	1.00
A	100	60	0.60
B	1,200	540	0.45
C	4,000	18,000	4.50
D	14,400	150,000	10.41
Cargo Ramp (Additional Penalty)			3
Total MMH/FH			19.97

Thus, even with conservative estimates and an additional maintenance penalties, the MMH/FH is well below the RFP required 24 [1]. Notable penalties applied was a flat 3 MMH/FH to service our complex cargo door, as well as increasing the scaling factor for the D check given the presumed difficulty to service the internal structure between the skin and pressure vessel. Additional unscheduled maintenance and repairs will also contribute to the nonoperational time of the aircraft, but as the design stands, there is a margin for maintenance downtime, even barring the expected benefits of the digital twin system.

XV. Acoustics and Emissions

A. Acoustics

The design choice of a BWB presents unique challenges in balancing performance while maintaining acoustic regulation limits. The placement of the engines has an ultimate effect on the noise levels associated with them and the limits achieved for stage 5 into the next decade. Ideally, the engines should be placed as far away as possible from the edges of the airframe to mitigate noise. For an open rotor propulsion system, it has been shown that placement at a location 94 percent of the rotor diameter upstream of the blended wing body trailing edge [33]. However, the aerodynamic and performance characteristics must be carefully analyzed to ensure that the necessary lift efficiency of the propulsion system is not severely hindered. Another mitigation technique is the use of vertical tails, which can block some of the sideline noise produced by the engines [33].

The acoustic profile of Gravibus falls within the stage 5 aircraft noise standards shall be met based on [34]. The approach, lateral and flyover limits are plotted for Gravibus in Fig. 62.

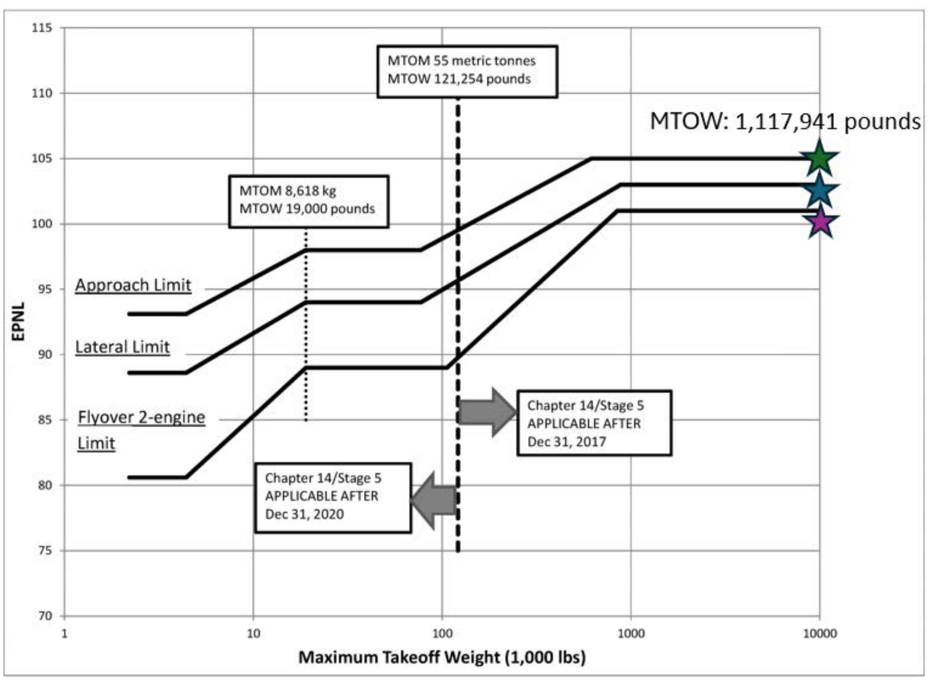

Fig. 62 Stage 5 Acoustic Profile of Gravibus

In addition, The GE90-85B meets the approach, lateral, and flyover limits are specified in the most up-to-date EASA Record under the ICAO Annex 16, Volume 1, Edition 8, Amendment 12, Chapter 3 [35] as shown in Table 52.

Table 52 GE90-85B Acoustic Profile

Noise level	Level [EPndB]	Limit [EPndB]
Lateral	95.4	101.2
Flyover	87.9	98.5
Approach	98.4	104.6

B. Emissions

The emissions profile of the GE90-85B is in compliance with the 14 CFR Part 34 fuel venting and exhaust emission requirements for turbine-powered airplanes. The exhaust emissions associated with the GE-90-85B are specified below [36]. Both the Standard Dual Annular Combustor (SDAC) and Low Emission Dual Annular Combustor (LEDAC) are considered in Table 53 based on [36].

Table 53 Comparison of Emission Rates

	SDAC	SDAC	SDAC	SDAC	LEDAC	LEDAC	LEDAC	LEDAC
Emission Rate [kg/h]	T/O	C/O	APP	IDL	T/O	C/O	APP	IDL
UHC	0.460	0.372	0.215	0.421	0.920	0.503	1.881	3.694
CO	1.71	1.49	3.37	14.40	0.920	1.12	17.81	46.00
NOx	539.40	332.00	51.30	6.00	597.30	376.90	31.50	6.10

C. Estimation of Gravibus Emissions Profile

The carbon monoxide emission profile was estimated for each mission profile using the unburned combustion reaction for octane, the primary compound in jet fuel, as shown below.

$$C_3H_{10} + 3.5O_2 \rightarrow 3CO + 4H_2O \tag{1}$$

Summarized below is the estimated lbs of carbon monoxide for each mission profile calculated by using stoichemistry and the pounds of fuel used for each mission segment. All mission segments except for the ferry mission exceed the reported pounds of carbon monoxide limit for the LEDAC GE90-85B [36] as shown in Table 54.

Table 54 Emissions Summary

Mission Segment	Carbon Monoxide Burned [lb]	GE90-85B LEDAC Carbon Monoxide [lb]
Maximum Payload	343.97	286.93
Mid Payload	631.63	544.32353
Ferry	369.12	899.43

XVI. Cost Analysis

A. Business case Analysis

As mentioned in the RFP, the cost analysis is done assuming a nominal production run of 90, 180, and 270 aircraft over 15 production years, which means the production run being analyzed will be based on the first 90 aircraft being produced in a 5-year period. Moreover, the flyaway production cost shall factor in a 10% profit margin per aircraft. All costs were tabulated into 2022 USD per the RFP - however, important costs are also tabulated as 2024 USD for convenience in the comparison with the current market situation. The cost analysis were done using several cost models, and their uncertainties and inaccuracies are discussed.

B. RDT&E and Unit Cost

The RDT&E and flyaway costs are calculated below based on the Roskam VIII and the DAPCA IV cost model from Raymer [3, 28]. Both methods were used for better understanding and analysis of the breakdown of RDT&E cost. The Roskam method uses calibrated numbers to 1989 while the Raymer method's model is calibrated to 2012. All cost analyses are therefore calibrated under the consideration of the inflation rate every year until the year 2022 using the U.S. Bureau of Labour Statistics CPI Inflation Calculator. 160 units for USAF and 20 units for niche level of commercial market were considered. Tables 55, 56, and 57 show the variables used for calculation and the estimated RDT&E and Flyaway costs using the two methods.

Table 55 RDTE Breakdown - Roskam

Cost Category	Cost(2022$)	Percentage (%)
Engineering	4,050M	11.88
Development Support	2,380M	6.98
Flight Test Airplane	2,640M	7.74
Flight Test Operations	4,640M	13.62
Test and Simulation	4,560M	13.39
RDTE Profit	2,280M	6.69
Cost to Finance RDTE	2,280M	6.69
Total Cost for 90 Aircraft over 5 years	50,900M	-

Table 56 RDTE and Flyaway Cost Breakdown - Raymer

Cost Category	Cost(2022$)	Percentage (%)
Engineering	7,348M	33.73
Tooling	3,730M	17.12
Manufacturing	6,331M	29.07
Quality Control	184M	0.85
Development Support	130M	0.60
Flight Test Cost	74M	0.34
Manufacturing Materials	2,960M	13.59
Engine Production	944M	4.34
Avionics	80,000,000	0.37
Total Cost for 90 Aircraft over 5 years in 2022 USD	48,566M	-

Table 57 Manufacturing Tool Costs per Hour

Labor Area	2012 USD per hr	2022 USD per hr	2024 USD per hr
Engineering	115	142.64	156.48
Tooling	118	146.36	160.56
Quality Control	108	133.96	146.95
Manufacturing	98	121.56	133.35

Table 58 shows the unit cost of Gravibus in each production timeline. The total program divided by the total number of aircraft gives us the unit cost of an aircraft which is 446 million USD. Applying the profit margin of 10%, the market price of the team's aircraft would be around 490 million USD at 15-year production line. The high RDTE cost for the team's aircraft is justified due to extensive research and development efforts required to bring a BWB design to work. The BWB configuration represents a significant departure from the traditional tube-and-wing body aircraft designs and therefore necessitates structural optimizations and advanced manufacturing techniques. The advanced avionics cost also contributed to the elevated RDTE costs. However, these investments are expected to pay off in the form of reduced operating costs, learning curves, and increased operational efficiency throughout the aircraft's long lifetime which will ultimately offset the initial high RDTE costs.

Table 58 Unit Cost with 10% profit margin per Production Timeline

90 A/C - 5years(2022$)	180 A/C - 10years(2032$)	270 A/C - 15years (2032$)
592.9 Million	530.2 Million	489.5 Million

C. Breakeven Analysis

As seen in Fig. 63, the breakeven point, where the total revenue equals the total costs, happens with the production of 136 aircraft in production. The team predicts that by the production timeline of 90 aircraft within the first five years, followed by 180 and 270 aircraft over same intervals, the fixed cost, quality of labor, and efficiencies in the production process will contribute reduction in the operating costs. Moreover, the long-term vision for the military project out-values the immediate profitability and will focus on establishing a sustainable and competitive presence in the US military market.

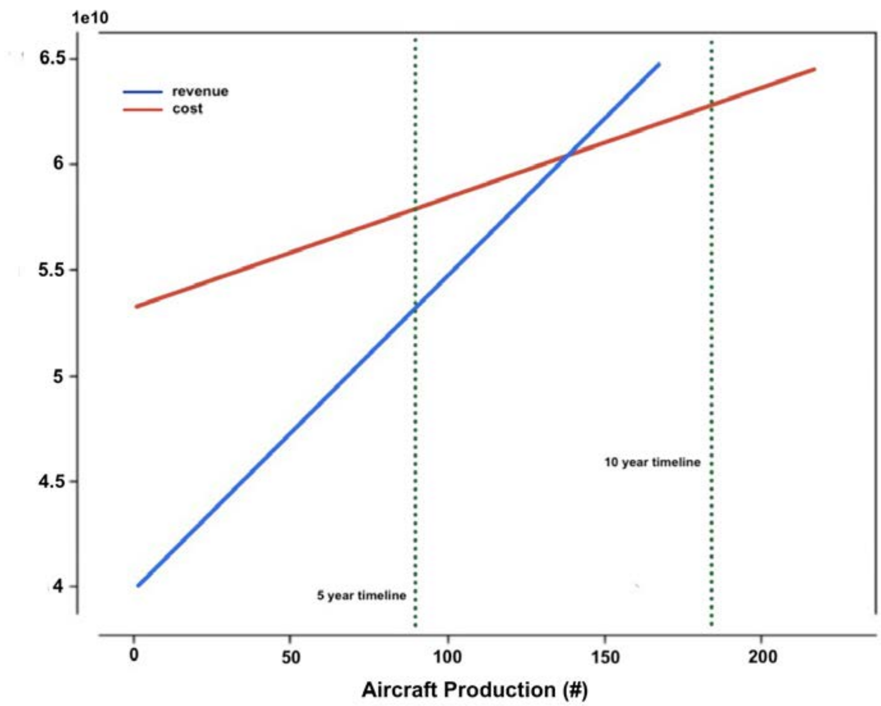

Fig. 63 Breakeven Point

Additionally, per the RFP, the development program is assumed to be a cost-share with the US DoD contribution. This cost-sharing arrangement with the US DoD would help to reduce the overall development costs for the manufacturer. Furthermore, the use of existing, proven technologies in commercial off-the-shelf and military-off-the-shelf systems will significantly reduce development costs and risks.

Considering these factors, it is reasonable to expect that the breakeven point could potentially be achieved within the first five years, as the government's cost-sharing and the use of commercial practices and off-the-shelf components would help in reducing the overall RDT&E costs.

D. Operating Cost

Direct operating costs were estimated using the Roskam VIII military airplane cost analysis method[28] and Nicolai Life Cycle Cost model[37]. Annual flight hours of 2,400 with a life span of 60 years were taken into assumption. As per the RFP, pilot, co-pilot, two loadmasters, and four additional back up relief crews were considered for the crew pay. The maintenance man hours per flight hour (MMH/FH) was tabulated as 20, which is no greater than the C-17 (20 MMH/FH) plus 20%. Table 59 and Fig. 64 show the total operating cost by flight hours assuming the total aircraft in service is the estimated product run. The operating cost per flight hour is mentioned at the very bottom.

Table 59 Operating Cost Breakdown

Cost Category	Cost($)	Percentage (%)
Fuel, Oil, and Lubricant	86,724M	35.08
Direct Personnel	61,112M	24.72
Indirect Personnel	29,147M	11.79
Consumable Materials	2,447M	0.99
Spares	3,263M	1.32
Depots	33,523M	13.56
Miscellaneous	1,706M	0.69
Total Operating Cost per year	247,218M	100
Operating Cost per flight hour(converted to 2022 USD)	76,500	-

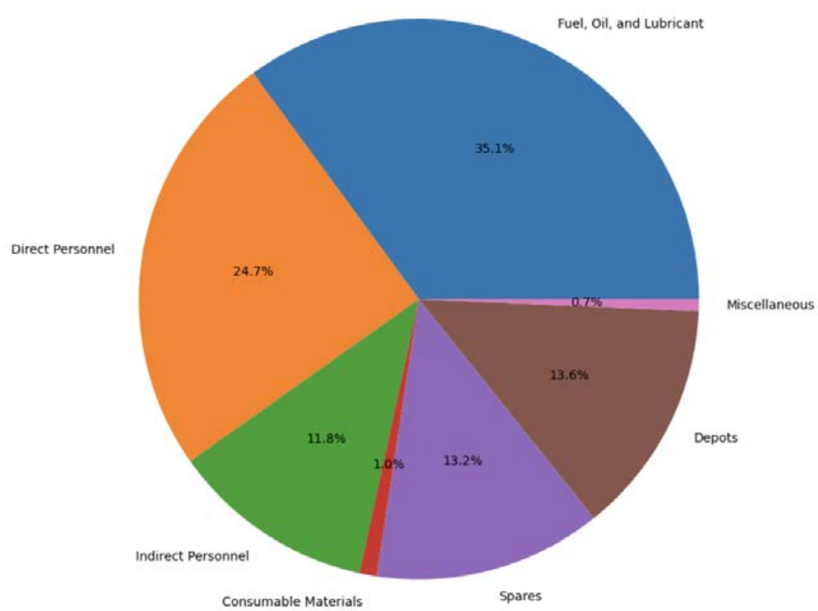

Fig. 64 Operational Cost Breakdown and Cost per Flight Hour

Figure 65 shows the operating cost per flight hour for USAF cargo aircraft. The source used was established based on 2020, therefore all the values were tabulated to 2022 USD for convenience in comparison. Additionally, for C-5, our primary aircraft for replacement with Gravibus, a value of 82,500 USD was used by averaging the cost over the past 10 years of its operation.[38]

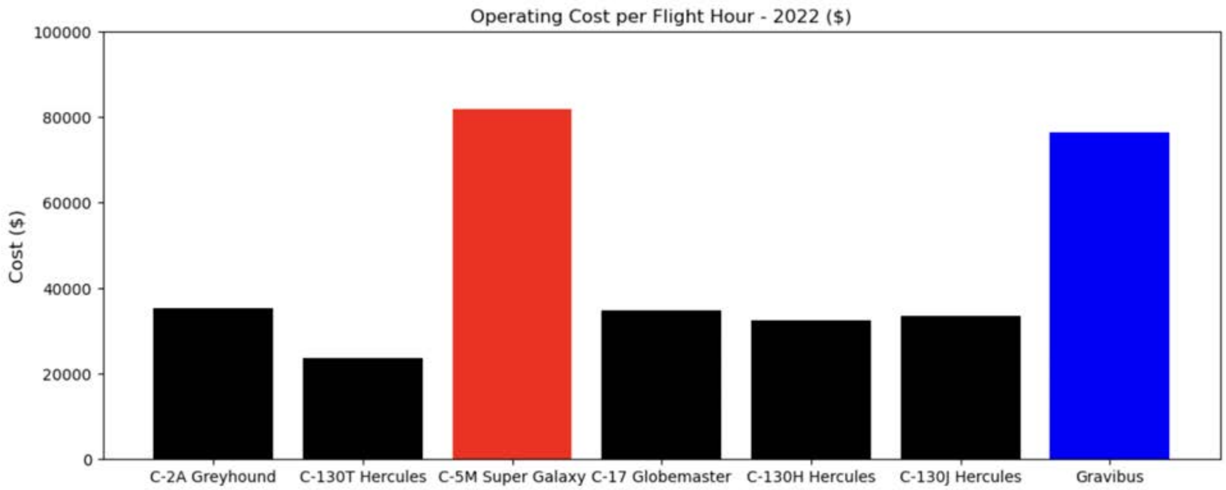

Fig. 65 Operational Cost Comparison

E. Comparison with C-5M

Compared to the C-5M, Gravibus offers lower operating cost per flight hour due to the aerodynamic efficiency and advanced systems integration. Its design offers 50% higher payload capacity, being able to transport 430,000 lbs of payload over range of 2,500 nautical miles. With proper maintenance, Gravibus assumes a service life of 60 years, which is significantly longer than the typical service life of legacy cargo aircraft. This extended service life will also help amortize the initial RDT&E costs over a longer operational period. These facts are summarized in Table 60. By implementing the proposed cost-saving strategies mentioned in Section XVI.F and leveraging the advantages of the blended wing body configuration, the team aims to establish a sustainable and competitive presence of Gravibus in the US military market.

Table 60 Cost Comparison to C-5

	C-5M	Gravibus
MTOW [lb]	840,000	1,160,000
Max Thrust per Engine [lb]	51,250	88,870
Range	2,150 nmi with 270,000 lb payload	2,500 nmi with 430,000 lb payload
Max Cargo [lb]	291,000	430,000
Unit Cost ($)	352M	489M
Operating Cost per Flight Hour ($)	≈ 82,500	76,500
Planned Sunset	2040	-

F. Cost Reduction Methods

1. Increase in production quantities

An increase in order quantities would spread the non-recurring costs for over more units which with significantly reduce the flyaway cost. Raymer's learning curve will further be studied and the learning curve for this team's aircraft will be proposed in FDR. Increasing the production quantities has a high chance of enabling multi-year procurement of aircraft components and materials at a reduced price. A trade study of total lifetime cost benefits of the seed aircraft will be also considered adding in FDR.

2. Optimization of RDT&E site

Conducting flight tests and development in low-cost geographic regions is another way to significantly lower the RDT&E cost. The team decided to conduct the RDT&E process in Huntsville, Alabama, depicted in Fig. 66, which has emerged as the ideal location due to its well-established aerospace ecosystem and numerous cost advantages. With major facilities like the U.S. Army Aviation, Missile Command, and NASA Marshall Space Flight Center, Huntsville provides access to diverse facilities, a skilled workforce, and potential collaborations.

Fig. 66 Aerospace Force in Alabama

Alabama ranks among the top states for low operational costs in the aerospace and defense sector, with its competitive cost of living, labor costs, and utilities, which would translate into significant cost savings for the Gravibus Project[39]. With pro-business policies, Alabama also offer a competitive business environment with attractive tax incentives such as a 25-year tax abatement program for aerospace and defense projects[40]. The location would also minimize the need for extensive training of the maintenance workers or relocation. The skilled workforce in aerospace and defense fields, enhanced by the presence of major aerospace employers and educational institutions like the University of Alabama will ensure a readily available talent pool.

G. Model Uncertainties and Inaccuracies

While the Roskam VIII and DAPCA IV from Raymer were used for the cost analysis for the aircraft, and although every cost value were calculated taking the US Consumer Price Index (CPI) factor into account, these models do not fully include the technological improvements and other factors that impact the total cost estimate. Similarly, the cost will be reduced as the timeline approach to the EIS due to technological advancement and maintenance crews' adaptability. Moreover, even though the Roskam VII method takes a lot of business factors into account, the cost of avionics and other miscellaneous items, including support equipment and cost of test facilities, are still vague and will need more research for a precise cost analysis. Additionally, the blended wing body design represents a significant departure from traditional aircraft configurations, and the cost models employed may not fully capture the cost drivers within this design.

XVII. Conclusions

The maturity of the current HLAs, the C-5M and C-17, necessitate the need for a new HLA for the USAF that is more capable and cost-effective as compared to both its predecessors and other proposed aircraft. Thus, the design of a novel BWB design, Gravibus, is presented in this report as a response to the RFP. Gravibus is capable of carrying a 430,000 lb payload to a range of 2,500 nmi, and can carry 3 M1A2 Abrams, 48 463L pallets, or 330 fully-equipped troops. To achieve these performance metrics, Gravibus features a high wing, twin tail design with a wing area of 6,000 sq. ft and an aspect ratio of 11.5. Four GE90-85B engines can provide up to 326,000 lbs of takeoff thrust while maintaining a cruise SFC near 0.568 lb/lb-hr. The design of Gravibus focused on minimizing operating costs including reducing the total amount of fuel required and optimizing access to key systems to reduce maintenance hours required. These operating costs, which are $ 76,500 per flight hour, reduce the total cost of the aircraft over its lifespan despite research and manufacturing costs which total to $ 490 million per aircraft. Gravibus differentiates itself from the competition primarily through the blended wing body design. Blended wing body aircraft can see improved lift-to-drag during cruise and a decrease in the thrust required - both of which serve to reduce fuel burn and result in significant cost savings. Further, the region beneath the cargo floor contains the vast majority of critical systems devices meaning maintenance is easier, faster, and thus less costly. Gravibus has more cargo capacity, a longer range, and is more cost effective as compared to the C-5M and thus would be the best replacement for the USAF to choose as its HLA to sustain its ability to effectively and rapidly deploy forces around the globe.

References

[1] "Heavy Lift Mobility Platform RFP," Retrieved from: https://www.aiaa.org/docs/default-source/uploadedfiles/membership-and-communities/university-students/design-competitions/2023-24-heavy_lift_rfp.pdf?sfvrsn=aecb7517_0, Last accessed on 5 February 2024.

[2] "MIL-STD-3013: Glossary of Definitions, Ground Rules, and Mission Profiles to Define Air Vehicle Performance Capability," Department of Defense, 2003.

[3] Raymer, D. P., *Aircraft Design: A Conceptual Approach Sixth Edition*, American Institute of Aeronautics and Astronautics, Playa del Rey, California, 2018.

[4] "C-5 Galaxy," Lockheed Martin, Retrieved from: https://www.lockheedmartin.com/en-us/products/c-5.html., Last accessed on 30 April 2024..

[5] "C-5M Super Galaxy," Air Force, Retrieved from: https://www.af.mil/About-Us/Fact-Sheets/Display/Article/104492/c-5m-super-galaxy/., Last accessed on 30 April 2024..

[6] "747-400/-400ER Freighters," Boeing, Retrieved from: https://www.boeing.com/resources/boeingdotcom/company/about_bca/startup/pdf/freighters/747-400f.pdf., Last accessed on 30 April 2024.

[7] Howe, D., "Blended wing body airframe mass prediction," College of Aeronautics, Cranfield University, Cranfield, Bedfordshire, UK, 2001.

[8] "Advisory Circular 117-1: Flight Member Rest Facilities," U.S. Department of Transportation, Federal Aviation Adminsitration, 2013.

[9] "Amendment to the Human Factors Design Standard: Chapter 10: Exhibit 10.4.8.3.1," U.S. Department of Transportation, Federal Aviation Adminsitration, 2006.

[10] "Engineering Design Handbook: Design for Air Transport and Airdrop of Materiel," US Army Materiel Command, 1967.

[11] "MIL-STD-209: Interface Standard for Lifting and Tiedown Provisions," Department of Defense, 2005.

[12] "Air Cargo Restraint Criteria," Aeronautical Systems Division, Wright-Patterson Air Force Base, 1973.

[13] El-Sayed, A. F., *Fundamentals of Aircraft and Rocket Propulsion*, Springer London, 2016.

[14] "Bypass Ratio," Retreived from: https://en.wikipedia.org/wiki/Bypass_ratio, Last accessed on 1 May 2024.

[15] "TYPE-CERTIFICATE DATA SHEET for GE90 Series Engines," General Electric Company, EASA, 2023.

[16] Meier, N., "Jet Engine Specification Database," Retrieved from: https://jet-engine.net/, Last accessed on 6 February 2024.

[17] "GasTurb," Retrieved from: https://www.gasturb.com/, Last accessed on 02/08/2024.

[18] Siddappaji, K., "Benefits of GE 90 Representative Turbofan through Cycle Analysis," Retrieved from: https://www.researchgate.net/publication/323790787_Benefits_of_GE_90_representative_turbofan_through_cycle_analysis#:~:text=In%20addition%20to%20the%20highest,today's%20high%20bypass%20ratio%20engines., November 17, 2008.

[19] "Flightstream Aerodynamic Modeling Software," Retrieved from: https://www.darcorp.com/flightstream-aerodynamics-software/, Last accessed on 1 May 2024.

[20] Paterson, J. H., "Aerodynamic Design Features of the C-5A," *SAE International*, 1968.

[21] Faegan, R. C., and Morrison, W. D., "Delta method, an empirical drag buildup technique," Tech. rep., NASA, 1978.

[22] Nelson, R., *Flight Stability and Automatic Control*, McGraw Hill, 1998.

[23] "Civil Jet Aircraft Design," Retrieved from: https://booksite.elsevier.com/9780340741528/appendices/data-a/table-1/table.htm, Last accessed on 1 May 2024.

[24] Torenbeek, E., *Synthesis of Subsonic Airplane Design*, Springer, 1976.

[25] "Code of Federal Regulations," *Title 14: Aeronautics and Space Chapter 1, Subchapter C, Part 25*, edited by FAA, Title 14, FAA, 2024.

[26] "MatWeb Material Property Data," Retrieved from: https://www.matweb.com/search/DataSheet.aspx?MatGUID=a0655d261898456b958e5f825ae85390, Last accessed on 4 March 2024.

[27] "Difference between Monocoque and semi-monocoque structures," Retrieved from: https://www.linkedin.com/pulse/difference-between-monocoque-semi-monocoque-structures-elangovan-m-xk7gc/, Last accessed on 30 April 2024.

[28] Roskam, D. J., *Airplane Design Part III: Layout Design of Cockpit, Fuselage, Wing and Empennage: Cutaways and Inboard Profiles*, DARcorporation, 2018.

[29] "Aircraft Tire Data Book," The Goodyear Tire and Rubber CO, Retrieved from: https://www.aps-aviation.com/wp-content/uploads/goodyear-aircarft-tire-data.pdf, 2002.

[30] Attaran, M., and Celik, B. G., "Digital Twin: Benefits, use cases, challenges, and opportunities," *Decision Analytics Journal*, Vol. 6, 2023.

[31] Spickler, S. S. E., "Home station checks keep C-17s mission ready," Retrieved from: https://www.dvidshub.net/news/416712/home-station-checks-keep-c-17s-mission-ready, Last accessed on 4 March 2024.

[32] "Types of Aviation Maintenance Checks," Retrieved from: https://www.naa.edu/types-of-aviation-maintenance-checks/, Last accessed on 4 March 2024.

[33] Yueping Guo, R. H. T., "System Noise Assessment of Blended-Wing-Body Aircraft with Open Rotor Propulsion," American Institute of Aeronautics and Astronautics, 2015.

[34] "Stage 5 Airplane Noise Standards," Retrieved from: https://www.federalregister.gov/documents/2017/10/04/2017-21092/stage-5-airplane-noise-standards, Last accessed on 4 March 2024.

[35] "TYPE-CERTIFICATE DATA SHEET FOR NOISE for Boeing 777," The Boeing Company, EASA, 2023.

[36] Balli, O., "Cost formation of exhaust emissions for GE90 turbofan engines used on commericial aircrafts," , 2018.

[37] Raymer, D. P., *Fundamentals of Aircraft and Airship Design*, Leland Malcolm Nicolai, 2010.

[38] Association, A. I., "Report No. GAO-23-106217," Tech. rep., Government Accountability Office, 2020.

[39] Association, A. I., "2020 Facts and Figures: U.S. Aerospace and Defense," Tech. rep., American Institute of Aeronautics and Astronautics, 2020.

[40] Park, C. R., "Huntsville: A Hive of Activity in Aerospace and Defense," *Decision Analytics Journal*, 2020.